Naval Research Laboratory

Washington, DC 20375-5320

NRL/MR/5660--12-9393

Estimating an Image's Blur Kernel from Edge Intensity Profiles

LESLIE N. SMITH

Applied Optics Branch
Optical Sciences Division

August 1, 2012

REPORT DOCUMENTATION PAGE

Form Approved
OMB No. 0704-0188

1. REPORT DATE *(DD-MM-YYYY)*	**2. REPORT TYPE**	**3. DATES COVERED** *(From - To)*
01-08-2012	Memorandum	

4. TITLE AND SUBTITLE

Estimating an Image's Blur Kernel from Edge Intensity Profiles

5a. CONTRACT NUMBER

5b. GRANT NUMBER

5c. PROGRAM ELEMENT NUMBER

6. AUTHOR(S)

Leslie N. Smith

5d. PROJECT NUMBER

5e. TASK NUMBER

5f. WORK UNIT NUMBER

7. PERFORMING ORGANIZATION NAME(S) AND ADDRESS(ES)

Naval Research Laboratory, Code 5665
4555 Overlook Avenue, SW
Washington, DC 20375-5320

8. PERFORMING ORGANIZATION REPORT NUMBER

NRL/MR/5660--12-9393

9. SPONSORING / MONITORING AGENCY NAME(S) AND ADDRESS(ES)

Office of Naval Research
One Liberty Center
875 North Randolph Street, Suite 1425
Arlington, VA 22203-1995

10. SPONSOR / MONITOR'S ACRONYM(S)

ONR

11. SPONSOR / MONITOR'S REPORT NUMBER(S)

12. DISTRIBUTION / AVAILABILITY STATEMENT

Approved for public release; distribution is unlimited.

13. SUPPLEMENTARY NOTES

14. ABSTRACT

This paper presents a simple and fast method to estimate the blur kernel model, support size, and its parameters directly from a blurry image rather than relying on the standard models. Also, this method estimates the parameters without the need to search the parameter space. In addition, this edge profile method is local and can provide a measure of spatial variation. The main insight of this work is that the profile of a blurry edge in an image is equivalent to a cumulative distribution function, which is used to estimate the underlying blur kernel functional form and parameters. We show how to utilize the concepts behind the statistical tools for fitting data distributions to analytically obtain an estimate of the blur kernel that incorporates blur from all sources, including factors inherent in the imaging system. The validity of this method is demonstrated with idealized and standard images and then NIR, SWIR, MWIR, and Active IR imagery results are shown to be similar to results from state-of-the-art methods.

15. SUBJECT TERMS

PSF estimation Deconvolution Probability
Image restoration Statistics

16. SECURITY CLASSIFICATION OF:			**17. LIMITATION OF ABSTRACT**	**18. NUMBER OF PAGES**	**19a. NAME OF RESPONSIBLE PERSON**
					Leslie N. Smith
a. REPORT	**b. ABSTRACT**	**c. THIS PAGE**	UU	44	**19b. TELEPHONE NUMBER** *(include area code)*
Unclassified Unlimited	Unclassified Unlimited	Unclassified Unlimited			(202) 767-9532

Chapter 1

Introduction

Blurry and noisy imagery is a ubiquitous problem for cameras and sensors across the spectrum of applications, including consumer photography, surveillance, computer vision, remote sensing, medical, and astronomical imaging. Simple methods to obtain sharp imagery are a valuable asset to all of these applications.

Although there are many sources of image blurring, blurring can be modeled by a single blur kernel, which is also called a point spread function (PSF). An equation for describing the observed blurry and noisy image as a function of the underlying sharp image is

$$b = h \otimes i + n \tag{1.1}$$

where b is the observed blurry image, h is the blur kernel, $\otimes$ is a convolution, i is the sharp image, and n is noise.

Fig. 1.1 gives a pictorial representation of the blurring component of equation 1.1. It is reasonable to assume the *edges in the real, continuous scene being imaged are step edges of discontinuous intensity*, such as on the left-hand side in Fig. 1.1. However, what is observed is a blurry image containing edge intensity profiles such as on the right-hand side of Fig. 1.1. Simple, approximate (i.e., "back-of-the-envelope") methods have long been an integral part of the scientific method [1; 2] and this report shows that the size and shape of the blur kernel can be quickly estimated from the edge profile.

In the overwhelming majority of real-world situations only the blurry image is available. Solving for the sharp image is an ill-posed problem because theoretically there can be an infinite set of blur kernel and sharp image pairs that produce the blurry image. Therefore, knowing the blur kernel defines the sharp image.

One solution in the literature [3] is to use standard models for the PSF, such as a linear blur kernel for motion blurring, a circular PSF for defocus, and a Gaussian PSF for atmospheric blur. In addition to choosing a functional form, one must guess at the parameters or perform parameter fitting. The edge profile method removes the guesswork and offers a way to quickly obtain a functional form, support size, and parameter values.

The solution of the image deblurring/restoration problem has been an active area of research for decades. Much recent research is in the area of blind deconvolution (see [4; 5]). Blind deconvolution attempts to iteratively solve for both the PSF and the sharp image from a blurry image by incorporating general knowledge of both the PSF and sharp image into an error function. These iterative methods are general but complex and computationally expensive.

The method described in this report falls in the gap between assuming a standard model for the PSF and the deconvolution methods. As this report will show, for little more than "back of the envelope", analytical computations, one obtains an approximate blur kernel that works well for some real-world imagery. Sections 2 and 3 show how to obtain an estimate of the blur kernel by using the concepts behind the statistical tools of probability plots, probability plot correlation coefficient (PPCC) plots, and quantile-quantile (Q-Q) plots. These simple methods can be used to estimate the PSF support size and functional form that caused the blurring in an image and then the parameters can be obtained without searching the parameter space. Section 4 shows the validity of this edge profile approach with idealized and a standard images and the deconvolution results using this method is shown to be similar to the results from state-of-the-art methods. Additional comparisons to state-of-the-art methods can be found in [6].

Manuscript approved December 23, 2011.

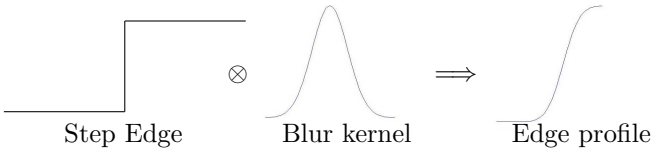

Figure 1.1: Step edges in the real-world are convolved with a blur kernel to produce the blurry edge profiles seen in imagery.

1.1 Main contribution

The main insight presented in this report is that *the profile of a blurry edge in an image is equivalent to the statistical cumulative distribution function,* which defines the underlying statistical probability density functional form. Similarly, in some circumstances the edge profile can be used to find an approximate blur kernel that represents the blurring of the scene in an image.

This report shows how to use the ideas behind the following statistical methods for data analysis:

1. Probability plot correlation coefficient plots can be used to select the blurring functional form or model that best matches the profiles of the blurred edges in the image.
2. Probability plots eliminates the search over the parameter space or the typical parameter fitting. The slope of a line or of the linear least squares fit determines the model parameters.
3. Edges can be compared, such as done with quantile-quantile plots or by global maps of the parameters, to determine the necessity of anisoplanatic (i.e., spatially varying) or asymmetric blurring (e.g., caused by linear camera motion) functions.

The benefits from using the concept behind these statistical methods for obtaining an image's blur kernel are:

1. This is a non-iterative method to estimate the PSF model for an image and its parameters. The blur kernel incorporates blur from all sources, including factors inherent in the imaging system and this method has the potential to estimate in real-time the blur kernel of each frame of a video.
2. An approximate kernel can provide intuitive insights, such as the blur spatial variation, or can be used to initialize more complex PSF estimation methods.
3. The algorithm rather than the user estimates the blur kernel support size and parameter values.

1.2 Related work

1.2.1 PSF estimation

There are many PSF estimation methods in the literature. The paper by Fergus *et al.* [7] describes one of the more accurate methods for estimating the blur kernel but it is also one of the most computationally demanding methods. The paper shows that a kernel can be estimated for blur due to camera shake by using natural image statistics together with a variational Bayes inference algorithm. This algorithm has been demonstrated to work well in a number of cases and it is used as a benchmark for comparison in this report. However, even for small images or when Fergus's method uses only a portion of an image, the solution is highly computationally intensive. The authors provide Matlab source code of this method via their project website that was used in the results section as a benchmark.

The recent paper by Cho *et al.* [8] presents a method for estimating the PSF using the same assumption of step edges before blurring as in this report. The authors use techniques of image reconstruction from projections for estimating the blur kernel. Their insight is that a line integral of the blur kernel can be considered as a convolution of the kernel with an image of an ideal line. They use the inverse Radon transform, which is used in image reconstruction, to reconstruct the PSF. However, in its current implementation the user must provide the edge profile length, which requires a parameter space search since this parameter value affects results. Our

approach is simpler and faster even though it can not solve for they types of complex kernels that their method can. They also present a Maximum a Posteriori (MAP) method that incorporates the Radon transform as a prior to help solve for both the kernel and image. This method slower and works in more situationsl but is actually an iterative blind deconvolution technique rather than a blur kernel estimation. Similarly, the edge profile method can be used as a prior within the MAP methodology. The authors provide Matlab source code of both these method, which was used in the results section for comparisons.

Joshi, *et al.* [9] detect edges in a blurry image and estimate the PSF under the assumption of a step edge before blurring, as is done here; however, they use an iterative Maximum a Posteriori (MAP) approach while we provide a analytic solution for the blur kernel. Furthermore, while they strive for a super-resolved blur kernel, our blur kernel is described by a continuous function.

Chiang and Boult [10] present a super-resolution algorithm including image restoration with a local blur estimation. Their edge model is the same as shown in Fig. 1.1. They assume a truncated Gaussian blur kernel but their solution is based on only two pixel values rather than the full edge profile. Furthermore, their solution is not in terms of a linear fit as can be obtained by using a quantile function. Barney-Smith [11] solves for the PSF by a parametric fit of data for the calibration of scanners. Her paper discusses the PSF and corresponding edge spread function (ESF), which is the same as the quantile function utilized in this work. However, she does not attempt to linearize the edge profile and uses an iterative gradient descent matching method to obtain the parameters.

Kayargadde and Martens [12] describe a method to compute a Gaussian blur kernel, σ_b, from polynomial coefficients. However, this method requires decomposing an image into Gaussian windowed subsets and σ_b is expressed as a function of the windows σ, rather than the simple approach presented here. Chalmond [13] estimates the PSF function by a hierarchical, multi-resolution methodology using a non-linear Markov random field model. He assumes that a reasonable representation of the sharp edge is given by a lower resolution version of the blurred image. Rosenfeld and Kak's book [14] introduced the idea of estimating the blur kernel from the edge blurring.

1.2.2 Blind deconvolution

Blind deconvolution methods simultaneously solve for both the blur kernel and the sharp image. Blind deconvolution is most often solved iteratively by minimizing an error function containing $\|b - h \otimes i\|$ plus other terms incorporating desirable characteristics of the blur kernel and sharp image. Within a single iteration these methods refine the PSF given the current best guess for the sharp image, and then solve for the best sharp image given the new PSF. However, noise in imagery compounds the difficulty of obtaining a solution, which is out of proportion to its relatively small size. A survey paper by Kundur and D. Hatzinakos [4] describes many of the techniques in blind deconvolution.

The paper by Shan, *et al.* [15] presents an iterative algorithm to remove motion blur from a single image. They present a probabilistic model for the blur kernel and sharp image and solve a MAP problem iteratively and alternately solve for kernel refinement and the sharp image. A focus of their paper is a new spatially random model for noise that they claim helps to recover the true blur kernel. However, the edge profile method is more robust in the presence of noise and does not require a specific noise model. Furthermore, their model is geared for handling camera motion and the edge profile method is more general. Executables of both their blind and non-blind deconvolution method are available on the authors' project website, so these were used in this research for comparisons.

The paper by Levin, *et al.* [5] analyzes and evaluates blind deconvolution algorithms and uses a MAP approach to estimate the blur kernel. They also demonstrate that a MAP approach with a sparse prior favors a delta function blur kernel when applied to finding the sharp image but is still useful for estimating the PSF.

A fast motion deblurring method is described in the paper by Cho and Lee [16] . This method introduces a prediction step and utilizes intensity derivatives rather than intensities. They obtained good results at a fraction of the execution time of other blind deconvolution methods. The authors made available an executable of their C program, which was used for some of the comparisons in this report.

Some approaches assume there are multiple images available [17]. Yuan *et al.* [18] use a pair of images, one blurry and one noisy, to facilitate capture in low light conditions. The approach in this report works on one image and even one slice through one edge in one image.

1.2.3 Non-blind deconvolution

Non-blind deconvolution methods solve for the sharp image assuming an accurate blur kernel is known. Hence, methods of accurately estimating the blur kernel are required in order to provide input for the non-blind deconvolution methods. There is an abundant literature on the non-blind deconvolution and the reader is referred to Lagendijk, *et al.* [3] for an introduction to this field.

Traditional methods such as Weiner filtering and Richardson-Lucy deconvolution [19], [20] are still widely used in many image deblurring tasks. Yuan, *et al.* [21] present a progressive inter-scale and intra-scale approach called a joint bilateral Richardson-Lucy algorithm that reduces image artifacts and attain sharp edges. This method uses both the latest restored image from the previous scale and the blurry image as guides in the iterative solution.

In [22], Levin, *et al.* describe a regularization technique using a sparse, natural image prior. This sparse method produces excellent results by encouraging the majority of image pixels to be piecewise smooth. The authors provide Matlab source code on their project website, which was used in the results section to deblur images using estimated blur kernels.

Chapter 2

Probability Plots and Blur Functions

This section provides background on the statistical methods that can be applied to the problem of estimating a blur kernel. These statistical methods are based on the relationships between probability density functions, cumulative distribution functions, and quantile functions. Once again, the basic insight of this work is that the edge intensity profile is equivalent to the cumulative distribution function. The first step is to determine the statistical model that best fits the data. Probability plot correlation coefficient (PPCC) plots allow one to select the blurring functional form that best matches the profiles of the blurred edges in the image. Given the functional form, the next step is to determine the governing parameters. The slope and intersection of a linear least squares (LS) fit to the quantile function values in a probability plot determines the parameters without necessitating a search the parameter space. Section 3 will show how to obtain the edge profile, which this section assumes is available.

2.1 Quantile-Quantile plots, Probability Plots, and Probability Plot Correlation Coefficient plots

For an ordered set of data y_i, for $i = 1$ to n, the quantile fraction is $p_i = (i - 0.5)/n$ and the quantile function is equal to y_i. A quantile-quantile (Q-Q) plot is constructed by sorting each of two datasets from smallest to largest and then plotting them against each other. In the case of a different number of values in each dataset, the dataset with the greater number of values is interpolated to the quantile fraction of the smaller dataset.

Sorting isn't necessary when comparing edge profiles because of our basic assumption that the edge intensity profile resembles the cdf. So a Q-Q plot is simply a plot against each other of the quantile function evaluation of each pixel in the edge profile of two different edges. When a different number of pixels are taken from the two edges, interpolation can be performed. For example, suppose x_j has n elements and y_i has m elements and $n > m$. We plot y_i against x_j where $j = \frac{n}{m}(i - 0.5) + 0.5$. When j is not an integer, we need to interpolate between the two nearest integer x_j.

The probability plot, which is also called a theoretical quantile-quantile plot, is a graphical technique for assessing whether a dataset follows a given distribution. This is a Q-Q plot where one of the quantile functions is the inverse of the theoretical cdf. The probability plot compares the distribution of the data to a theoretical distribution function, and the data should form a straight line if it conforms to the function and depart from a straight line if not.

Here we consider the profile of the edge to be the empirical cumulative distribution function of the data and compare it to theoretical cdfs in a search for the best functional form and parameters. The governing model could be found by minimization of the least squares error between the edge profile and the theoretical cdfs but this would require a search of the parameter space. Using the quantile function eliminates this search and the parameters are easily found as the slope and intercept of a single linear least squares fit. As described in the context of data analysis on page 199 of Chambers, *et al.* [24]: "What we have established, really, is that a single theoretical quantile-quantile plot compares a set of data not just to one theoretical distribution, but simultaneously to a whole family of distributions with different locations and spreads." In essence, the linearity of the quantile function values can be used as a measure of the appropriateness of the functional form. In addition,

the quantile function transforms the curved edge profile to a straight line where a closed form linear LS fit is quick to compute.

Since the data will fall on a straight line if the underlying model is correct, a measure of linearity of the probability plot indicates the appropriateness of a functional form for a blur kernel. The Pearson product-moment correlation-coefficient is a measure of linearity and is often used in probability plot correlation coefficient (PPCC) plots [23]. It is given by

$$CC = \frac{\sum_i (x_i - \bar{x})(y_i - \bar{y})}{\left[\sum_i (x_i - \bar{x})^2 \sum_i (y_i - \bar{y})^2\right]^{1/2}} \tag{2.1}$$

where CC is the correlation coefficient, $\bar{x}$ and $\bar{y}$ are averages of datasets x_i and y_i. In the PPCC plots, x_i is replaced by the theoretical quantile function, such as those in Table 2.1.

Some probability distributions are not a single distribution but are a family of distributions due to one or more shape parameters. These distributions are particularly useful in modeling applications since they are flexible enough to model a variety of datasets. Construction of the PPCC plot is done by plotting the linearity measure, such as CC in equation 2.1, as a function of the shape parameter. The maximum value corresponds to the best value for the shape parameter. The goal is to obtain a functional form that best matches the blurry edge profile's shape.

More details on these tools are available in the book "Graphical Methods for Data Analysis" [24].

Table 2.1: Common probability distribution functions (pdf) that may be considered as functional forms for a blur kernel. Associated cumulative distribution functions (cdf) and quantile functions (qf) are also shown.

Distribution	pdf / PSF	cdf	qf
Gaussian	$\frac{1}{\sqrt{2\pi}\sigma} exp\left[-\left(\frac{x-\mu}{\sqrt{2}\sigma}\right)^2\right]$	$\frac{1}{2}\left[1 + erf\left(\frac{x-\mu}{\sqrt{2}\sigma}\right)\right]$	$\mu + \sigma\sqrt{2} erf^{-1}(2p-1)$
Uniform	$\frac{1}{b-a}$ for $a \le x \le b$	$\frac{x-a}{b-a}$ for $a \le x \le b$	$a + p(b-a)$ for $0 \le p \le 1$
Triangular	$\begin{cases} \frac{2(x-a)}{(b-a)(c-a)} & \text{for } a \le x \le c \\ \frac{2(b-x)}{(b-a)(c-a)} & \text{for } c \le x \le b \end{cases}$	$\begin{cases} \frac{(x-a)^2}{(b-a)(c-a)} \\ 1 - \frac{(b-x)^2}{(b-a)(c-a)} \end{cases}$	$\begin{cases} a + \sqrt{(b-a)(c-a)p} \\ b - \sqrt{(b-a)(c-a)(1-p)} \end{cases}$
Logistic	$\frac{exp\left[-(x-\mu)/\sigma\right]}{\sigma\left(1+exp\left[-(x-\mu)/\sigma\right]\right)^2}$	$\frac{1}{1+exp\left[-(x-\mu)/\sigma\right]}$	$\mu + \sigma ln\left(\frac{p}{1-p}\right)$
Cauchy	$\left(\pi\sigma\left[1 + \left((x-\mu)/\sigma\right)^2\right]\right)^{-1}$	$\frac{1}{\pi} arctan\left((x-\mu)/\sigma\right) + \frac{1}{2}$	$\mu + \sigma tan[\pi(p - \frac{1}{2})]$
Tukey λ	Computed numerically	Computed numerically	$\begin{cases} log(p) - log(1-p) \text{ if } \lambda = 0 \\ [p^\lambda - (1-p)^\lambda]/\lambda \text{ otherwise} \end{cases}$

2.2 Blur functions

Table 2.1 contains some common probability distribution functions that have also been used in the past as blur kernels [11]. More sophisticated methods for finding a generalized functional form can be explored by utilizing techniques in the vast literature on statistical distributions, such as in references [25; 26].

The Gaussian function is one of the most common functions used, both for the pdf and the PSF. The Gaussian pdf, cdf and qf are given in Table 2.1 where μ is the mean, σ is the standard deviation and erf is the error function. Searching the parameter space is eliminated because the mean and standard deviation are easily determined from the intercept and slope of the probability plot. Hence, if it is known for a blurry image that the blur kernel is a Gaussian function, it is only necessary to apply the erf^{-1} function to the edge profile to determine σ. Similarly, if it is known that the blur kernel's functional form matches any of the single distributions functions listed in Table 2.1, their quantile function will help determine the parameters for these blur kernels

It is desirable to compare the blurry edge profile to a family of distributions to find the most appropriate functional form. By plotting the correlation-coefficient for various values of the functional shape parameter λ, the value of λ that best matches the edge profile can be taken as the proper functional form. The last entry in Table 2.1 is the Tukey lambda distribution, which is a family of distributions governed by a shape variable λ. For the Tukey lambda distribution, if

- λ = -1: distribution is approximately Cauchy
- λ = 0: distribution is exactly logistic
- λ = 0.14: distribution is approximately normal
- λ = 0.5: distribution is U-shaped
- λ = 1: distribution is exactly uniform

In other words, the value for λ in a PPCC plot that produces the maximum value indicates if the best fit functional form is one of these distributions. The Tukey lambda distribution family was used for the work in this report because it models the most common functions used for blur functions but there are other distribution families that merit investigation [25]. Furthermore, one can match the edge profile with combinations of quantile functions [26].

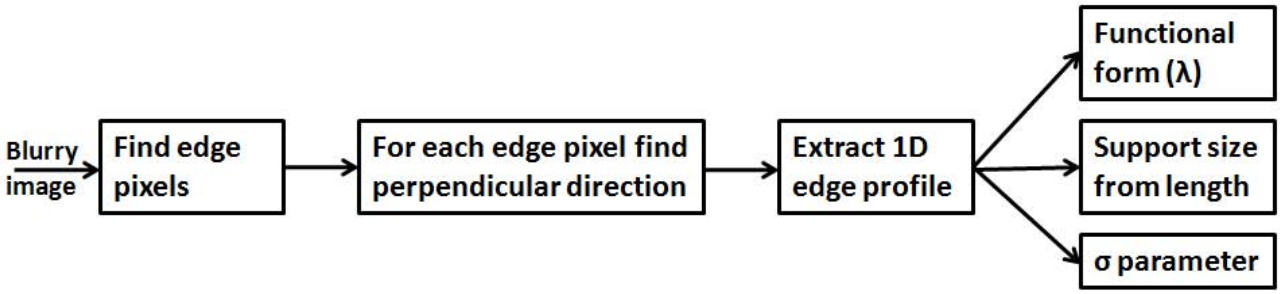

Figure 3.1: Top level flowchart of the blur kernel modeling algorithm

Chapter 3

Determining the blur kernel

As illustrated in Fig. 3.1, this technique starts with a blurry image and finds appropriate edge pixels. Appropriate edge pixels separate relatively high contrast, homogeneous regions. Section 3.1 will describe an algorithm to automatically qualify edge pixels, determine the direction perpendicular to the edge, and assess if the surrounding regions are locally homogeneous. As Fig. 3.1 shows, the next step is to extract the 1-D edge profile that transverses from one homogeneous region to the other homogeneous region, which is also discussed in section 3.1. Once the edge profile has been selected, the blur function model and parameters that best fit the data can found as described in Sections 3.2 and 3.4.

3.1 Automatically extracting edge profiles

Edge profiles can be manually extracted by the user or performed automatically by the system. Manual extraction is more robust to noise than automatic methods but automatic methods are necessary for independent systems. Hence this author experimented with several ways to automatically extract an edge intensity profile. [Including testing the method in Cho, *et al.* [16].]

Automatically extracting edge profiles is done by selecting appropriate edge pixels, determining the perpendicular direction, and finding endpoints for the profile. There are several requirements for an edge pixel to produce a reasonable result. The edge should separate locally homogeneous regions that are of significantly different intensities. If the contrast isn't significant, the estimation of the blur kernel will be more sensitive to noise distortion. If the regions on both sides of the edge are not homogeneous, the image details will distort the result.

The algorithm to automatically extract edge profiles in an image is as follows:

1: Perform an edge detection.
2: Compute a derivative map.
3: Compute a noise threshold from the derivative map.
4: **for** each detected edge pixel **do**
5: Compute an energy in each of four directions.

6: Compute the perpendicular direction.
7: Determine the edge profile length.
8: Test the edge profile to reject or accept
9: Solve for parameters.
10: **end for**

Tests indicate that the results are insensitive to the edge detection method. In this work Matlab's implementation of Canny's method was used with larger than default thresholds in order to limit the edge pixels to h/igh contrast edges. A derivative map is a map of the differences in intensity between neighboring pixel; that is, it is equal to $\mid H \mid + \mid V \mid$ where H is a horizontal filter and V a vertical filter. For example, H could be the filter (-1 1) and $V = H^T$. The noise threshold was computed from homogeneous regions, which are regions in the derivative map with locally small values.

There are several ways to determine edge direction, such as by structure tensors. For this work, an energy is computed in each of four directions from an edge pixel; horizontal, vertical, and the two diagonal. This is done by summing the derivative map values stepping away both ways from the edge pixel in each of these four directions and stopping when the derivative values fall under the noise threshold. The edge direction is determined as the direction with the greatest energy and the perpendicular direction is 90 degrees from edge direction.

The question of how to determine the proper edge profile length was investigated and several alternative methods were compared. In the absence of noise, the definition of the profile endpoint is where the gradient of the pixel difference becomes zero or changes sign. However, in the presence of noise it generally does not work to rely on this definition. The adopted method for estimating the endpoint pixel is to compare intensities differences (i.e., average gradient) between three locations: at the edge pixel, a user input maximum length of the profile and half-way between. Then it is determined from the average gradient which half is likely to contain the endpoint and this bisection procedure is repeated within the chosen half until the endpoint pixel is determined. If the edge profile is accepted, the parameters are computed by the algorithm presented in the next section.

3.2 Solving for the best blur function model and its parameters

It is straightforward using the edge profile for determining the best blur function and resolving its parameters. As shown in Fig. 3.1 the edge profile is input to both the PPCC plot and the probability plot computation. If the edge profile matches a cdf profile such as in Table 2.1 , then substituting the edge intensity values into the corresponding quantile function should yield a straight line.

The algorithm for the PPCC plot is given by:

1: Linearly transform the edge profile.
2: **for** $-1 \leq \lambda \leq 1$ **do**
3: Compute the quantile function values.
4: Compute a linear least squares fit.
5: Compare qf to LS line via equation 2.1.
6: **end for**
7: Plot the correlation coefficient versus λ.

Since a cdf function is always in the range from 0 to 1, a linear transform of the edge profile values to this range is required. The edge profile is actually transformed to the range $\frac{0.01}{n}$ to $1.0 - \frac{0.01}{n}$, where n is the number of pixels in the edge profile. Reducing the endpoints by $\frac{0.01}{n}$ prevents infinities at 0 and 1 and is similar to the technique described in Chambers, *et al.* [24]. The quantile function values are computed for each pixel in the edge profile. Then the results of the quantile function are compared using equation 2.1. This correlation coefficient (CC) value is then plotted against the value of shape parameter λ and the maximum CC value indicates the best blur function. Examples of a PPCC plot are shown in Fig. 4.2.

Once the functional form is chosen, the algorithm for obtaining the scale parameter σ is similar to the PPCC plot algorithm. It is given by:

1: Linearly transform the edge profile.
2: Take the quantile function for each pixel on this line.
3: Do a linear least squares fit.
4: $\sigma = 1/slope$
5: **if** horizontal or vertical profile **then**

6: $\sigma = \sigma/\sqrt{2}$
7: **end if**

Again the linear transform of the edge profile is to the range $\frac{0.01}{n}$ to $1.0 - \frac{0.01}{n}$. After performing the linear least squares fit, σ is obtained as the inverse of the slope of this line. The division by $\sqrt{2}$ is necessary since diagonal distances differ from horizontal or vertical distances by $\sqrt{2}$.

3.3 Assumptions

The edge profile method assumes the blur kernel can be reasonably approximated by an analytical function and specifically by the family of distribution functions being used (i.e., Tukey-lambda). This assumption is less stringent than the standard model's assumption of the blur being approximated by a specific analytical function, wherein lies a virtue of this method.

Since the edge profile method estimates one dimensional slices of the blur kernel in the directions perpendicular to the edge, this method makes assumptions about the nature of the two dimensional kernel. As stated in Rosenfeld and Kak [14], page 273: "If there is reason to believe that the PSF is circularly symmetric, then H(u,v) is also circularly symmetric, so that it needs only to be known along one radial line for it to be known everywhere." This assumption is reasonable for certain problems, such as defocused blur problems where there is no reason for directional dependence. In addition, the nature of atmospheric turbulence blurring is random so on average it is reasonable to assume the blur kernel is approximately circularly symmetric. In this work, if profiles from edges in different orientation were similar, an approximate circular symmetry was assumed. For example, a similar 1-D Gaussian profile in both the horizontal and vertical directions implied a circular 2-D Gaussian PSF.

In the case of motion blur, the kernel is assumed to be approximately one dimensional in the direction of the blur, in which case the profile contains sufficient information to define the blur kernel. Edge profiles in the four primary directions (horizontal, vertical, 2 diagonals) will indicate the nature of the blur; for example, if it is approximately circularly symmetric or the direction of the motion blur. Therefore, the edge profile method is applicable in cases wherever the standard models are appropriate but the method is not applicable to problems of handling random blur or where the assumptions stated in this paragraph are clearly violated.

Although this edge profile method is local and permits computing spatially varying blur kernels, the scope of the results in this report is limited to the case of a constant PSF throughout the image. The vast majority of the papers in the literature assume a constant PSF for the entire image. Furthermore, the Fergus method is used as a comparative benchmark in this report and is performed only on a sub-region in the image, which relies on the constant PSF assumption. For the edge profile method, the constant PSF assumption allows one to examine any strong vertical and horizontal edges in the image to estimate a blur kernel for the entire image. Hence the functional form, size and parameters determined at a few strong edges can be used to design a blur kernel for the entire image.

3.4 PSF support size

Most PSF estimation and blind deconvolution methods require as input an estimate of the size of the blur kernel. It is easily shown that the length of the edge profiles provides an estimate of the PSF support size. This can be seen by imagining a 1-D step edge that is convolved with a square wave of length X. The result is a ramp edge of length X. Hence, if the length of the ramp edge profile is X, the support size of the underlying blur kernel is also X. Another viewpoint is that the extent of the effects of a blur kernel is reflected in the size of the edge profile.

In practice, the edge profile lengths mostly fall into a range of values. A good choice for PSF support size tends to be close to the top end of the range. Choosing a reasonable PSF size is critical for uniform blur kernels. On the other hand, a Gaussian PSF is governed more by σ and the size need only be large enough to include significant kernel values (rule of thumb is a size of about 4σ). However, if the edge profile method determines that the blur kernel can be modeled by a Gaussian, the length of the profile provides an additional estimate of σ (the edge length divided by 3 or 4).

Using the edge profile to guide PSF size prevents one from choosing too large a size and reduces the amount of needless computation during blur kernel estimation or deconvolution. Furthermore, parsimony suggests that the blur kernel size be made as small as possible but not smaller.

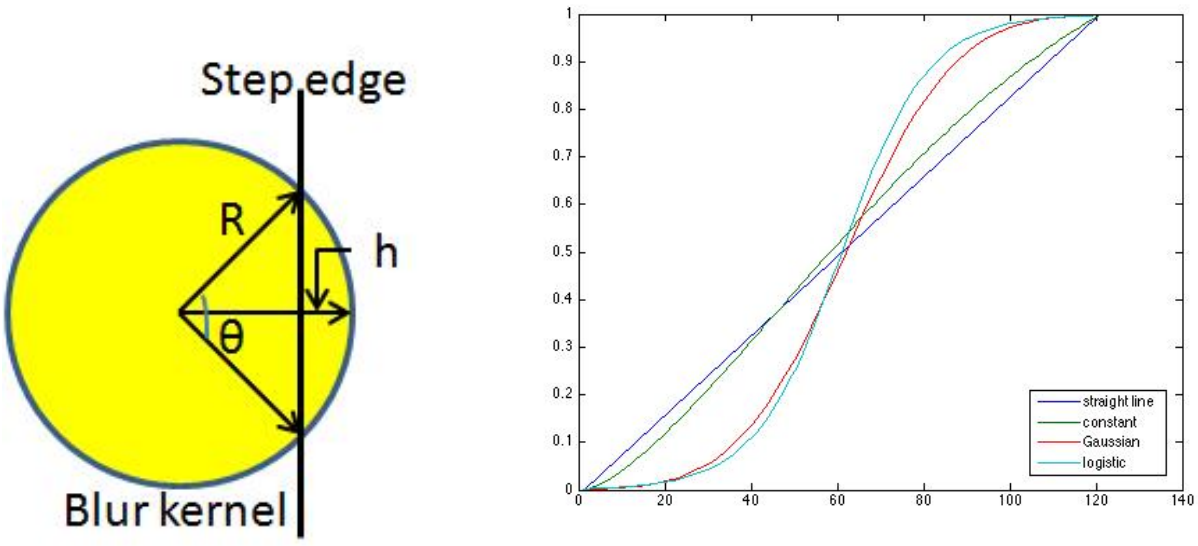

(a) (b)

Figure 3.2: (a) Model of a symmetric blur kernel interacting with a step edge (b)Resulting analytical edge profile assuming a circularly symmetric blur kernel interacting with a step edge in the continuous domain.

3.5 Analytical verification

It is possible to analytically verify the edge profile method results in a few simple cases. In the case of a 1-D kernel interacting with a perpendicular step edge, it is obvious that the kernel components is obtainable from the edge profile. Since the cdf is obtained as the integral/sum of the pdf, it follows that the pdf can be found from the cdf by differentiation/subtraction. Here one simply takes the pixel differences along the edge profile as the kernel components and normalize them so the sum equals one.

Here we work in the continuous domain and show results for three circularly symmetric cases; a constant kernel, Gaussian kernel and logistic. The same analysis can be performed for other cases too. Fig. 3.2a illustrates the model with a circularly symmetric blur kernel. With no loss of generality, assume the step edge with zeros on the left side and ones on the right.

First assume a constant blur kernel. The resulting convolution of the kernel will be proportional to the area of the kernel overlapping the right side of the edge. Hence the value for the edge profile will be proportional to h shown in Fig. 3.2a. The angle θ can be computed as $\theta = 2\arccos((R-h)/R)$, where R is the radius of the kernel and h is the overlap with the edge. Then the area is computed as the fraction of the circle enclosed by the two cords and the arc, minus the area of the two triangles:

$$profile = \frac{\theta R^2}{2} - (R-h)R\sin\frac{\theta}{2} \tag{3.1}$$

As it turns out, even though the blur kernel is constant, the edge profile is close to but not quite constant. An example is shown in Fig. 3.2b.

The next case is a circularly symmetric Gaussian blur kernel. Here we use these equations with $\mu = 0$ and $\sigma = 1$

$$\frac{1}{\sqrt{2\pi}}\int_0^t e^{-x^2}\,\mathrm{d}x = \frac{1}{2}erf(\frac{t}{\sqrt{2}}) \tag{3.2}$$

$$\frac{1}{\sqrt{2\pi}}\int_{-\infty}^{\infty} e^{-x^2}\,\mathrm{d}x = 1 \tag{3.3}$$

In 2-D, the profile when the edge is on the right side of the step edge/kernel overlap is found by integration of

$$profile = \frac{1}{2\pi}\int_h^\infty e^{-x^2}\,\mathrm{d}x \int_{-\infty}^\infty e^{-y^2}\,\mathrm{d}y = \frac{1}{2}\left[1 - erf\left(\frac{h}{\sqrt{2}}\right)\right] \tag{3.4}$$

A similar result is obtain when the edge is on the left side of the kernel. Hence, the result is the same as the Gaussian cdf shown in Table 2.1 and in Fig. 3.2b.

Finally we show the results using a circularly symmetric logistic blur kernel. Again we use assume $\mu = 0$ and $\sigma = 1$. The blur kernel is

$$PSF = \frac{e^{-R}}{\pi(1+e^{-R})^2} \tag{3.5}$$

When the edge is on the right side of the kernel and $r = R - h$ is the distance of closest edge point to the kernel center, then the profile is found by integration

$$profile = \frac{1}{\pi}\int_0^{2\pi}\int_r^\infty \frac{e^{-R}}{\pi\left(1+e^{-R}\right)^2}\,\mathrm{d}R = \frac{1}{2}\left[1 - \frac{1}{1+e^{-r}}\right] \tag{3.6}$$

A similar result is obtain when the edge is on the left side of the kernel. Hence, the result is the same as the logistic cdf shown in Table 2.1 and in Fig. 3.2b.

3.6 Estimating the blur kernel; from point source to corners

It is well known that the blur kernel can be estimated from the imagery of a point source; for example see [14], page 272: "if there is any reason to believe that the original scene contains a sharp point, then the image of that point in the degraded picture is the PSF. This would be the case in an astronomical picture, where the image of a faint star could be used as an estimate of the PSF."

What is not well known and I have yet to find an example in the literature, is that if the original scene contains a corner on a homogeneous background, then the image of that corner can be used to estimate the the PSF. To this author's knowledge, there isn't an example in the literature on obtaining the PSF from an image of a corner. However, the corner result is analogous to the point source case, so I will start with a simple case of a point source. Say a 3x3 blur kernel

$$k_{i,j} = \begin{bmatrix} k_{1,1} & k_{1,2} & k_{1,3} \\ k_{2,1} & k_{2,2} & k_{2,3} \\ k_{3,1} & k_{3,2} & k_{3,3} \end{bmatrix}$$

is convolved with the original scene that is a point of value 1 on a background of zeros,

$$\begin{bmatrix} \cdots & \cdots & \cdots & \cdots & \\ \cdots & 0 & 0 & 0 & \cdots \\ \cdots & 0 & 1 & 0 & \cdots \\ \cdots & 0 & 0 & 0 & \cdots \\ \cdots & \cdots & \cdots & \cdots & \end{bmatrix}$$

then the result will be

$$\begin{bmatrix} k_{3,3} & k_{3,2} & k_{3,1} \\ k_{2,3} & k_{2,2} & k_{2,1} \\ k_{1,3} & k_{1,2} & k_{1,1} \end{bmatrix}$$

The resulting image of the point is a rotation of the blur kernel.

In a similar manner, if we have the same 3x3 blur kernel as above but the original scene has a corner with intensity 1 in the bottom right on a background of zeros, then the result will be

$$\begin{bmatrix} 0 & 0 & 0 & \cdots & \\ 0 & k_{3,3} & k_{3,3}+k_{3,2} & k_{3,3}+k_{3,2}+k_{3,1} & \cdots \\ 0 & k_{3,3}+k_{2,3} & k_{3,3}+k_{2,3}+k_{3,2}+k_{2,2} & k_{3,3}+k_{2,3}k_{3,2}+k_{2,2}+k_{2,1}+k_{3,1} & \cdots \\ 0 & k_{3,3}+k_{2,3}+k_{1,3} & k_{3,3}+k_{2,3}+k_{3,2}+k_{2,2}+k_{1,2}++k_{1,3} & 1 & \cdots \\ 0 & \vdots & \vdots & \vdots & \cdots \end{bmatrix}$$

where the kernel is normalized to sum to 1. The values for the blur kernel can be estimated by examining pixel difference within the region from the corner corresponding to the size of the blur kernel, in this case 3 pixels. If we name these intensity value $I_{i,j}$ such that

$$I_{i,j} = \begin{bmatrix} I_{1,1} & I_{1,2} & I_{1,3} \\ I_{2,1} & I_{2,2} & I_{2,3} \\ I_{3,1} & I_{3,2} & I_{3,3} \end{bmatrix}$$

This allows for a simple way to determine the first few kernel values:

$$k_{3,3} = I_{1,1}; k_{2,3} = I_{2,1} - I_{1,1}; k_{3,2} = I_{1,2} - I_{1,1}; k_{2,2} = I_{2,2} - I_{2,1} - I_{1,2} + I_{1,1}$$

The last formula can be generalized for finding the kernel value for all the remaining kernel elements. That is, the equation is

$$k_{i,j} = I_{i,j} - I_{i,j-1} - I_{i-1,j} + I_{i-1,j-1} \tag{3.7}$$

This demonstrates the proof of concept that the blur kernel elements can be estimated from the image of a corner on a flat background.

Fortunately, this idea can be generalized in several ways. It is obvious that if the original scene background intensity is greater than zero and the corner intensity differs from 1.0 that scaling will transform that image into an equivalent situation. What is not as obvious is how this works if the corner is not a perfect 90 degree corner. This is possible if one knows the shape of the corner in the original scene. If one assumes that a map,

$$M_{i,j} = \begin{cases} 1 & \text{if pixel i,j belongs to the corner} \\ 0 & \text{if pixel i,j is part of the background} \end{cases}$$

is available or can be inferred from the observed image, then

$$k_{i,j} = I_{i,j} - \sum_{ii,jj}^{i,j} M_{ii,jj} \times k_{ii,jj} \tag{3.8}$$

where $k_{i,j}$ is initialized to zero before the summation.

However, several attempts to utilize this theory on the imagery in this report failed to produce a blur kernel that worked reasonably well to deblur the image. I assume there is something I am missing and until found this method will not work properly. It is being recorded in this report simply as a reminder of the work and the need to determine the missing elements.

3.7 Power law gradient for noise versus edges

The author conducted some research related to this topic of image restoration. In a plot of the log of the frequency histogram of the gradients, it is noticeable for a wide range of imagery there are two near linear parts, as can be seen in Figure 3.3a. In this figure, the gradients are computed as the difference between a pixel and the one below it. The center values, which are near zero, are primarily due to noise throughout the image. Since noise occurs in almost every pixel, its frequency is relatively higher than gradients due to true edges or image details. Furthermore, noise frequency drops off quickly as the its magnitude increases.

On the other hand, the frequency of gradients from true image details are of larger magnitude and less frequent than noise. The most interesting aspect of Figure 3.3a is that a straight line can be drawn through the part of the histogram of edge gradients, as is shown in this figure. The straight line fit is qualitatively good over most of the range of gradient values. Similarly, a straight line can be drawn through the points near zero, with a similar good fit but over a smaller range. The value of this analysis is to obtain a good threshold of gradient magnitude between noise and image details, which is useful information in a variety of applications. For example, many denoising algorithms require the noise σ and this method is a good way to estimate an unknown variance.

Furthermore, a feature of log plots is that polynomial functions become straight lines. Hence the frequency of the noise magnitude and the frequency of the image details magnitude are obeying different power laws. The slope of the lines indicate the power of the function relating magnitude to frequency of occurrence (line slopes for the Lena image = -0.028, -0.035).

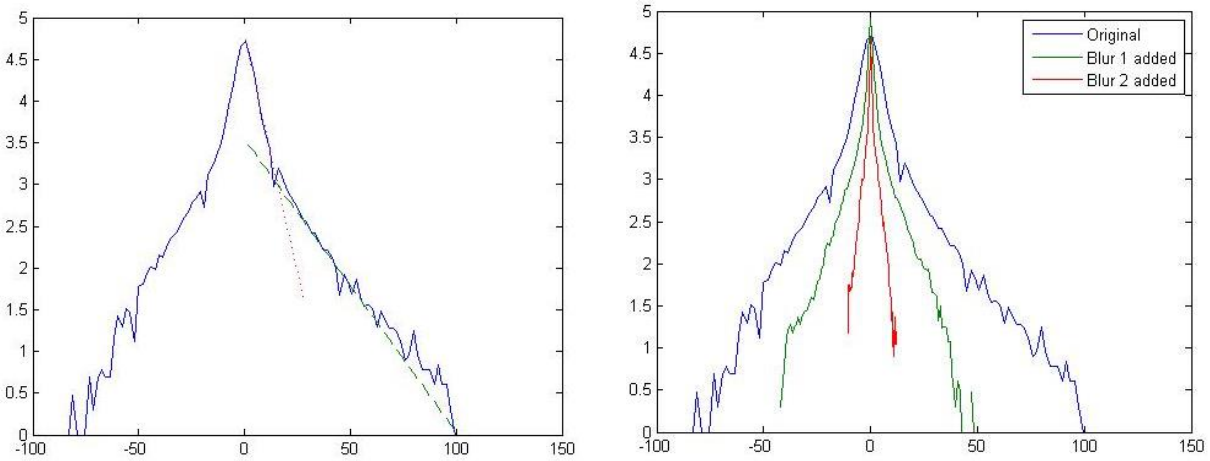

(a) (b)

Figure 3.3: Plot of the log of the frequency histogram of the gradients in the standard Lena image. (a) The original image. Two dashed/dotted lines illustrate the fit of the two linear areas of this curve (line slopes = -0.028, -0.035). (b) Comparing the original gradient magnitude profile to collapsed versions from the image blurred.

Figure 3.3b compares this gradient profile as the image becomes blurry. With even a small amount of blur, the gradient magnitude profile "collapses" towards zero. One way to look at the objective of image restoration is to restore this gradient magnitude profile. Clearly some of the information in the original image is lost by the blurring, especially near the noise/edge threshold of the original image. However, Figure 3.3b gives another avenue to restoring a blurry image via a new regularization term.

One also obtains similar results to that shown in Figure 3.3a by computing the second derivative or other forms of computing the first derivative. Furthermore, adding noise to an image changes this curve in predictable ways; the sharp peak at zero flattens and the curve near zero becomes fatter. The results in this section apply generally to natural images, as can be seen in the plots of gradients over many images, such as contained in Fergus, *et al.* [7] and Shan, *et al.*. [15].

Chapter 4

Results

First, we demonstrate the viability of the edge profile method by describing the results on a synthetically blurred step-edge image. Once the effectiveness of the technique is shown for this idealized image, the algorithms are applied to a synthetically blurred standard cameraman and Lena images. The results from the automation process of Section 3.1 are shown and compared to state-of-the-art methods. Next, examples of defocused and one dimensional motion blurring of an NIR bar chart image is described. Then the results of processing a defocused outdoor SWIR image example is given. Finally, the full methodology is applied to two sets of real-world imagery (MWIR and active IR) where blurring was caused by atmospheric turbulence.

In this section we make use of an implementation of the algorithm for calculating the Structural SIMilarity (SSIM) index between two images [27]. This is an image quality metric based on a high quality reference image. Visually comparing two images is approximate and highly subjective but using the SSIM quality metric allows for an objective comparison. We compare the sharpened imagery results using the blur kernel estimated by the above edge profile methodology, to the results utilizing other ways to estimate the PSF. In particular, in this section the PSF is estimated in one of six ways: the edge profile method, the Fergus method, the Radon transform, RadonMAP [8] or three blind deconvolution techniques. With the first two methods, the estimated PSF is then input into a non-blind deconvolution method. We also show results from four non-blind deconvolution methods: Matlab's Lucy-Richardson (LR), Levin's sparse deconvolution (sparse 1) [22], Radon's sparse deconvolution (sparse 2) [8], and SJAs non-blind deconvolution [15]. The two implementations of the sparse deconvolution method, the original by Levin, *et al.* and a recent version by Cho, *et al.*, gave different SSIM results so both are included in the following results. The three blind deconvolution methods used are RadonMAP [8], SJA's, [15] and Cho's fast blind deconvolution [16] techniques.

Table 4.1: Evaluation of λ_{max} and the value of the corresponding correlation coefficient (CC) for various blurred ideal step image ($\sigma = 2$ where applicable). The first column give the functional form of the kernel used to blur the image. The second column give λ_{max} and CC (within parathesis) for the case of the blurry image. The third column is the case when noise is added to the blurry image.

Blurred with	λ_{max} (CC)	Noisy image λ_{max} (CC)
Logistic	0.05 (0.9999)	0.0 (0.9996)
Gaussian	0.15 (0.9998)	0.2 (0.9978)
U-shape	0.4 (0.9999)	0.4 (0.9993)
Uniform	1.0 (1.0)	1.0 (0.9993)

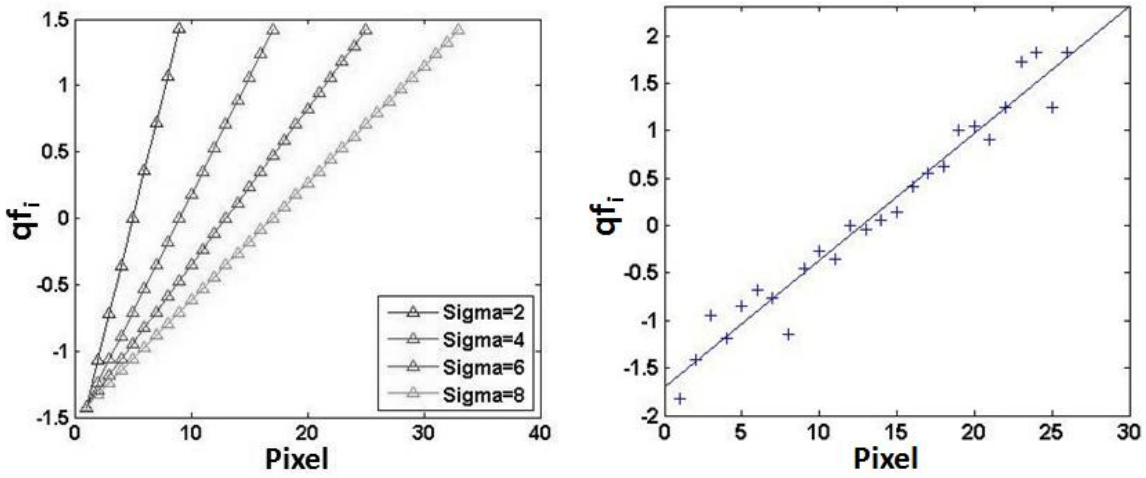

(a) (b)

Figure 4.1: Probability plots of Gaussian blurred ideal step edge. (a) Step edge images blurred with a Gaussian kernel with $\sigma = 2, 4, 6, 8$. (b) Step edge image blurred with a Gaussian kernel ($\sigma = 6$) and Gaussian white noise added (SNR = 35). The line is a linear LS fit to the data.

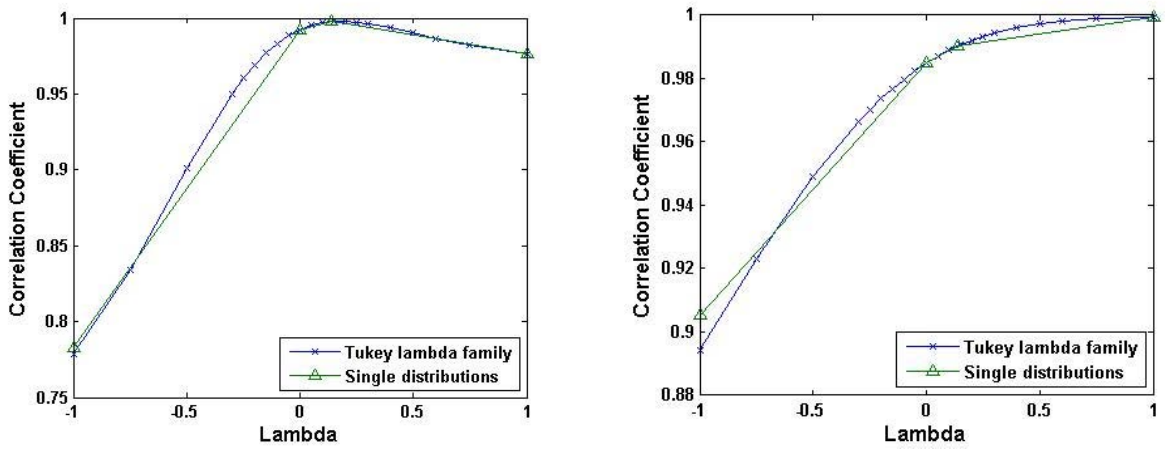

(a) (b)

Figure 4.2: PPCC plots for step-edge image with Gaussian white noise added (SNR=35). (a) blurred with a Gaussian kernel, $\sigma = 6$. (b) blurred with a linear, uniform kernel of length 8 pixels.

4.1 Tests on an ideal step image

The effectiveness of the edge profile method is first demonstrated on a simple 256x256 step-edge image, where the left half = 0 and the right half = 1, which is then blurred with a Gaussian kernel with a known σ. In the case with no noise, the transformed edge profile values fit perfectly to a straight line with the correct slope, as is shown in Fig. 4.1a for $\sigma = 2, 4, 6, 8$.

While it is clear that the method works when there is no noise, to be truly useful the method must prove to be robust to noise. Gaussian white noise (SNR=35) was added to a Gaussian blurred step-edge image ($\sigma = 6$). Fig. 4.1b shows the plot of edge profile pixels along with a linear least squares fit to the data. Even though the estimated σ result did vary somewhat due to the noise, over numerous tests the estimated σ generally remained within 3% of the the value used to blur the image. Furthermore, this accuracy was maintained over the range of

(a) (b) (c)

Figure 4.3: Deblurring a blurred cameraman image. (a) Cameraman image blurred with a Gaussian kernel, $\sigma = 6$. (b) Resulting deblurred image, using the estimated blur function (Gaussian) and parameter ($\sigma = 5.5$). (c) Close up of a sub-region of the blurry image (top-left), the deblurred sub-region using the edge profile PSF (bottom-left), the deblurred sub-region using the Fergus estimated PSF (top-right), and the deblurred sub-region using the SJA blind deconvolution (bottom-right). Estimated blur kernels for each method are shown as an inset.

blurring, $\sigma = 2 - 12$.

The automatic method described in Section 3.1 typically computes λ, σ, and length for several adjacent pixels. Since noise introduces a random error, taking the median of the estimated values within a local neighborhood reduces the noise effects. Tests on this noisy imagery indicate that the median of even ten local values improves the estimate for σ compared to picking an individual σ value.

Finally, we examine PPCC plots to see how effectively they determine the underlying functional form. The PPCC plot for the Gaussian blurred step-edge image is shown in Fig. 4.2a. Also plotted in Fig. 4.2a are the single distributions for Cauchy, logistic, Gaussian, and uniform blur kernels, which correspond to $\lambda = -1, 0, 0.14, 1.0$. The maximum of the correlation coefficient occurs at $\lambda = 0.15$, which matches well with the fact that the image was blurred with a Gaussian. For contrast, the PPCC plot for the step-edge image blurred by an linear, uniform blur kernel is shown in Fig. 4.2b. Here the maximum of the correlation coefficient occurs at $\lambda = 1.0$, as it should for a uniform blur kernel. However, it is not necessary to create the PPCC plot to obtain the maximum value for λ. Table 4.1 provides automatically obtained λ_{max} and the corresponding correlation coefficient for various blurred ideal step images. The first column gives the functional form of the kernel used to blur the image. The second column gives λ_{max} for each case of the blurry image. The third column is the case when noise is added to the blurry image. In this case of the blurry step image, the results from this method accurately reflect the functional form of the kernel used to blur the image. Note that the correlation coefficient's proximity to 1.0 is an indicator of the goodness of the fit of a functional form.

In summary, it was demonstrated in this section that the PPCC plot is capable of unearthing the underlying functional form and the probability plot is able to estimate σ.

4.2 Standard cameraman image

After evaluating the edge profile algorithms in Section 4.1 for a step-edge, we next validate them on a synthetically blurred standard image. Shown in Fig. 4.3a is the cameraman image that is blurred with a Gaussian kernel, $\sigma = 6$ and in Fig. 4.3b is the deblurred result of using the PSF estimated by the edge profile method and the non-blind deconvolution method described in Shan, *et al.* [15]. Fig. 4.3c contains a comparison of deblurring solutions using a sub-region of the the blurry image, which is shown in the top left. Estimated blur kernels for each method are shown as an inset in the corner of the deblurred image. In the bottom left is the deblurred sub-region using the Gaussian ($\sigma = 5.5$) blur kernel obtained from the edge profile method and a sparse non-

(a) (b) (c)

Figure 4.4: Deblurring a blurred cameraman image with the Radon transform method. (a) User required edge profile length, sliceSize = 23. (b) User required edge profile length, sliceSize = 19. (c) RadonMAP method with user required edge profile length, sliceSize = 23.

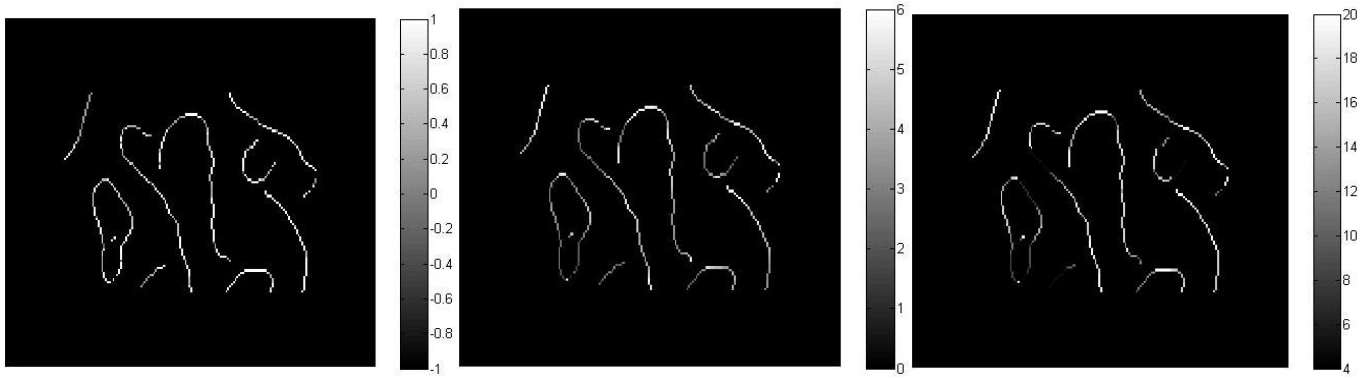

(a) (b) (c)

Figure 4.5: Parameter maps for a sub-region of blurred Cameraman image. The intensity scale is on the right-hand side and the intensity of the pixels correspond to their magnitude. (a) Lambda Map. (b) Sigma Map. (c) Length Map.

blind deconvolution method [22]. The Fergus estimated PSF [7] along with the sparse non-blind deconvolution method produced the image in the top-right corner. The deblurred sub-region and blur kernel estimate in the bottom-right corner was obtained from the SJA blind deconvolution [15]. The results from four deconvolution methods, which are Richardson-Lucy (RL), two sparse implementation [22; 8] and SJA's non-blind deconvolution, are visually similar.

The Radon transform method [8] was also used to deblur the cameraman image in Fig. 4.3a and the results are displayed in Fig. 4.4. The Radon transform parameter sliceSize, which is used as the profile length and PSF size, is a user supplied value and their results are strongly dependent on this value. In the author's current implementation, this sliceSize parameter must be determined by a parameter search. However, based on the edge profile length, we choose $sliceSize = 23$ and produced the PSF and image shown in Fig. 4.4a. This deblurred image displays strong ringing artifacts but a search of the parameter space for sliceSize and stdnoiseB (a smoothing parameter) lead to the improved image in Fig. 4.4b. Here the deblurred image contains fewer artifacts but the PSF is less similar to the Gaussian kernel that blurred the image. The RadonMAP method was also run on the blurry cameraman image and the results are shown in Fig. 4.4c. This deblurred image is better and does not have ringing artifacts.

Column two in Table 4.2 gives SSIM scores for the deconvolved image compared to the original cameraman

Table 4.2: Mean SSIM quality metric of the deblurred images relative to an idealized reference.

Technique	Blurry CM	Noisy CM	Blurry Lena	Noisy Lena
No deblurring	0.707	0.725	0.680	0.810
Edge profile PSF / RL	0.815	0.756	0.774	0.858
Edge profile / Sparse 1 [22]	0.819	0.820	0.796	0.886
Edge profile / Sparse 2 [8]	0.790	0.825	0.780	0.884
Edge profile/SJA non-blind	0.721	0.796	0.783	0.868
Fergus PSF / RL	0.752	0.743	0.754	0.858
Fergus PSF / Sparse 1	0.753	0.789	0.762	0883
Fergus PSF / Sparse 2	0.749	0.803	0.762	0.875
Fergus PSF / SJA non-blind	0.723	0.795	0.747	0.847
Radon transform / Sparse 1	0.730	0.812	0.761	0.887
Radon transform / Sparse 2	0.777	0.810	0.759	0.874
RadonMAP / Sparse 1	0.772	0.822	0.732	0.886
RadonMAP / Sparse 2	0.768	0.824	0.734	0.874
SJA blind deconvolution	0.743	0.375	0.742	0.846
Cho's blind deconvolution	0.682	0.714	0.716	0.804

Table 4.3: Summary of CPU times in seconds of each technique and imagery cited in this manuscript. CPU time is cited running on a 2.4GHz Intel dual Core CPU on a T61 Thinkpad with 4GB RAM. In most cases, the Fergus PSF estimation run was performed on sub-regions of approximately 200x200, rather than on the full image.

Technique	CM, Lena (512x512)	NIR (1024x1280)	SWIR (700x550)	MWIR (64x64)	Active IR (150x180)
Edge profile PSF	0.02 - 0.1	0.02 - 0.1	0.02 - 0.1	0.02 - 0.1	0.02 - 0.1
Fergus PSF[7]	970	1200	780	65	800
Sparse non-blind [22]	14	70	25	0.16	1.2
Matlab LR	6	51	9	.18	0.5
Matlab blind	13	120	20	0.26	1.6
SJA non-blind [15]	41	110	29	3	8
SJA blind [15]	65	240	62	6	12
Fast blind [16]	6.8	31	8.5	NA	1
Radon transform [8]	15	36	33	NA	16
RadonMAP [8]	150	NA	NA	NA	70

image. The SSIM index value between two images can be considered as the quality measure of an image if the other image (the reference) can be considered as perfect quality. If both images are identical the SSIM score equals 1.0 and goes to 0 as the match deteriorates. The blur kernels are estimated by the edge profile, Radon transform, RadonMAP, and the Fergus methods, then input to the four non-blind deconvolution method and the SSIM scores are listed in Table 4.2. In addition, the SJA and Cho's blind deconvolution methods were run on the blurry image and their scores listed in this table. In this case of the synthetically blurred cameraman image, the SSIM scores indicate that the edge profile method produces a better result, which is reasonable because this test case is designed to match the underlying assumptions of Section 3.3.

It is possible to run an edge detection to create a map of edge pixels, then run the edge profile method on every edge pixel. Doing this for the sub-region displayed in Fig. 4.3c one can create maps such as shown in Fig. 4.5. These maps illustrate which pixels were accepted for computation by the automatic edge extraction method and an estimate of its value (by its intensity) throughout the image. Experience has shown that it is useful to look at these three maps on important horizontal and vertical edges when estimating the PSF because they provide an overall sense of PSF symmetry and the validity of the isoplanatic assumption; that is, this indicates if it is reasonable to use a constant and/or symmetric PSF for the image. Fig. 4.5 indicates it is reasonable to use a constant PSF assumption for this image and the averages indicate the Gaussian functional form is appropriate. Grouping λ values in this map by direction of the edge one obtains an average $\lambda = 0.17$ for horizontal edges and $\lambda = 0.19$ for vertical edges. Similarly, grouping σ values by direction of the edge one obtains an average $\sigma = 6.0$ for horizontal edges and $\sigma = 5.0$ for vertical edges. This gives the estimate of $\sigma = 5.5$, which was used to deconvolve the image. A map of edge profile lengths is shown in Fig. 4.5c and can be used to estimate the PSF support size that is appropriate. Grouping values by direction of the edge and we obtain an average length = 18.0 for horizontal edges and length = 15.0 for vertical edges. This implies that the effects of the Gaussian blurring is noticeable for about 15 - 18 pixels. However, the effects of the Gaussian function is primarily dictated by σ and the support size just needs to be large enough. A rule of thumb is to make the PSF support size about four times the σ value, which is about 22. For the result in Fig. 4.3 we used a 21x21 Gaussian PSF. Although the PSF estimated is not precise in this synthetically blurred example, the estimate reasonably matches the original blur kernel.

Furthermore, the CPU times for the various software is listed in Table 4.3. An unoptimized Matlab implementation of edge profile method executes orders of magnitude faster than any other method. The code to compute correlation coefficients for a range of λ values, find the maximum λ, and determine σ from the quantile function executes in only 0.02 seconds CPU time and the function for finding strong edges and extracting the profile runs in about 0.1 seconds (CPU time is cited running on a 2.4GHz Intel dual Core Thinkpad with 4GB RAM). This emphasizes the nature of the edge profile method as a quick but approximate (i.e., "back-of-the-envelope" or"quick and dirty") that is useful in itself or as a quick check on more accurate methods. On the other hand, obtaining a blur kernel estimate using the Fergus method on a sub-region of 170x170 pixels takes about 800 seconds. Please note that it is not a fair comparison to compare CPU times of a PSF estimation method to blind or non-blind deconvolution methods; the point to be made here is that the edge profile method is a very fast in a field where all other methods are compute intensive. This speed advantage is one of the core advantages of the edge profile method. This method is valuable as a "quick and dirty" estimation of the blur kernel, which makes it attractive even when it's performance is worse than the other methods. In addition, this method is preferable to guessing required in choosing a standard model and the searching of the parameter space for a best fit.

The presence of random noise in an image plagues attempts to deblur an image. As with all methods, the edge profile method is affected by noise and here we contrast the relative performance of this method to other methods. In Fig. 4.6a the standard cameraman image was blurred with a Gaussian blur kernel with $\sigma = 3$ and random, Gaussian white noise was added. Using the original cameraman image as the reference, this noisy cameraman image gives a score of SSIM = 0.725. The automatic method for finding several high contrast edges, extracting these edge intensity profiles, yielded a large range of $0.0 < \lambda_{max} < 0.4$ and $2.1 < \sigma < 2.8$. The error in the automatic method is due primarily to errors in correctly determining edge profile end-points. Although, the automated method for extracting an edge profile starts to fail as the noise level increases, the edge profile method works well if one manually extracts edge profiles, which in this case correctly found $\lambda_{max} = 0.15$ implying a Gaussian blur function, with $\sigma = 2.7$. Hence, a 13x13 Gaussian blur kernel, with $\sigma = 2.7$ was used as input to the non-blind deconvolution methods. The deblurred image is shown in 4.6c and the SSIM results shown in column three of Table 4.2.

(a) (b) (c)

Figure 4.6: Deblurring a noisy, blurred cameraman image. (a) Cameraman image blurred with a Gaussian kernel, $\sigma = 3.0$ with white noise added. (b) Resulting deblurred image, using the estimated blur function (Gaussian) and parameter ($\sigma = 2.7$). (c) Close up of a sub-region of the noisy, blurry image (top-left), the deblurred sub-region using the edge profile PSF (bottom-left), the deblurred sub-region using the Fergus estimated PSF (top-right), and the deblurred sub-region using the SJA blind deconvolution (bottom-right). Estimated blur kernels for each method are shown as an inset.

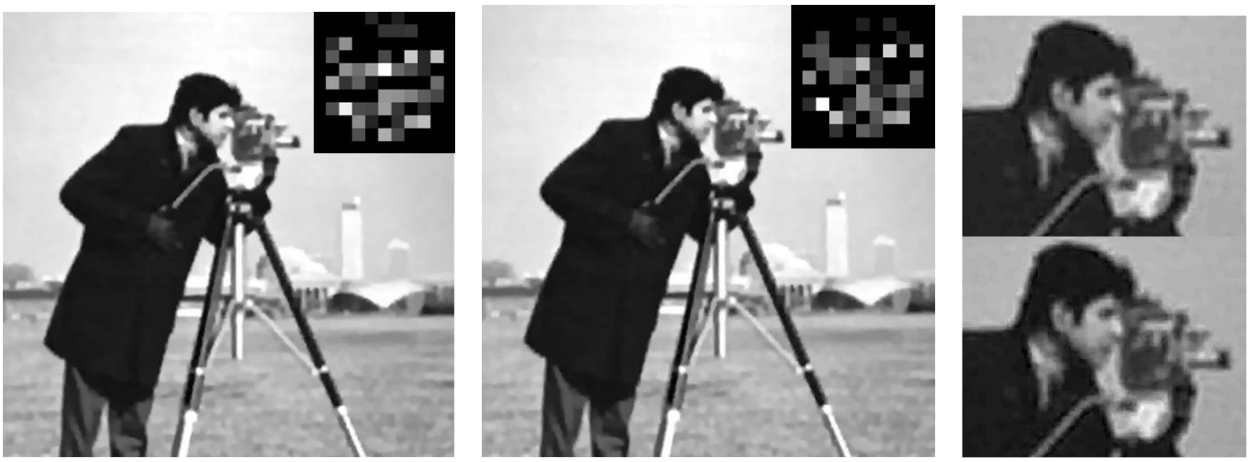

(a) (b) (c)

Figure 4.7: Deblurring a noisy and blurry cameraman image with the Radon transform method with sliceSize = 11. (a) Radon transform. (b) RadonMAP method. (c) Close up of a sub-region; top is Radon transform result, bottom is RadonMAP result.

Initially the Fergus PSF estimation worked poorly but with significant parameter tuning it was possible to obtain good results. Since each run of the Fergus method is computationally expensive, as shown in Table 4.3, this parameter search and testing of different sub-regions required many hours of computer time. The best result is displayed in Fig. 4.6c. The SSIM results using this PSF as input to the four non-blind deconvolution methods is shown in column three of Table 4.2. In addition to the parameter tuning, it is noteworthy that significantly different blur kernels were obtained by running the Fergus method on different sub-regions. This variation is likely caused by the presence of the random noise.

The Radon transform and the RadonMAP results are displayed in Fig. 4.7. Some tuning of the implementation's stdnoiseB parameter was necessary to find the proper level for smoothing the noise but as can be seen in the figure, the results are good. This is also reflected in the SSIM scores in column three of Table 4.2. Table 4.3 lists the CPU time for the Radon transform and RadonMAP methods. The speed of the Radon transform is

noteworthy as one of the faster blur kernel estimation methods, with the exception, of course, of the edge profile method.

The blind deconvolution blur kernel and resulting image for the SJA method are shown in Fig. 4.6c. As visible here, it is not unusual for the noise to be amplified in both the kernel and in the deblurred image. Table 4.2 shows the SSIM scores for two blind deconvolution methods and it is clear that these methods have significant difficulty in the presence of noise.

In summary, the presence of random noise caused the automated edge profile extraction to improperly estimate the endpoints, leading to a wide range of parameter results. However, manually extracting an edge profile does lead to identifying the correct blur kernel function and parameters. After significant parameter and sub-region tuning the Fergus's method was able to produce results of good quality. The Radon transform and RadonMAP methods performed well, despite of the presence of the noise. But the two of the blind deconvolution methods amplified the noise, leading to visibly worse results. The overall impression is that some methods are more sensitive to the presence of noise than others.

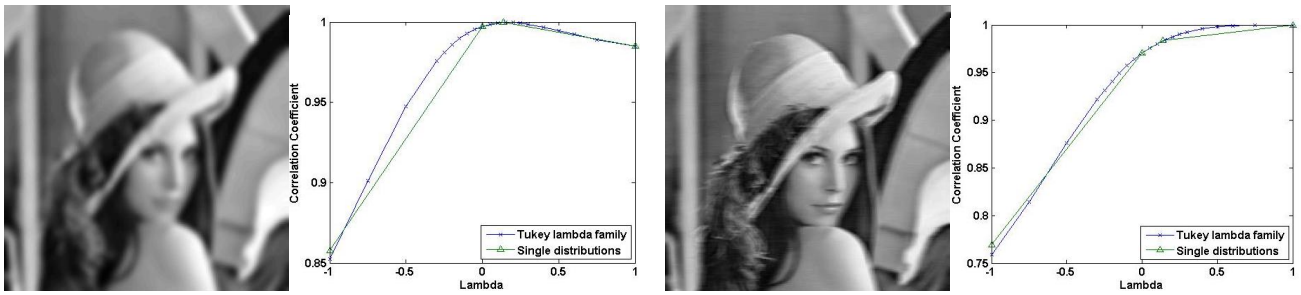

(a) (b) (c) (d)

Figure 4.8: (a) Gaussian blurred Lena image. (b) PPCC plot of Gaussian blurred Lena image. (c) Motion blurred Lena image. (d) PPCC plot of motion blurred Lena image.

(a) (b) (c) (d)

Figure 4.9: (a) Result from SJA non-blind deconvolution using a 27x27 Gaussian blur kernel with $\sigma \simeq 5.4$ (see inset) from the edge profile PSF estimation. (b) Result from SJA non-blind deconvolution using the Fergus's PSF estimation. (c) Result from SJA blind deconvolution. Inset shows estimated PSF. (d) Result from Cho's Fast blind deconvolution.

4.3 Standard Lena imagery

In this section, PSF estimators, non-blind and blind deconvolution methods are compared using a standard Lena image synthetically blurred with a known blur kernel. Shown in Fig. 4.8a is the result of blurring the Lena image with a Gaussian filter ($\sigma = 6$). A PPCC plot is used to model the functional form and is shown in 4.8b.

The maximum $\lambda_{max} = 0.15$ implies a Gaussian functional form, as it should in this case. In contrast, Fig. 4.8c shows the Lena image blurred with a 16 pixel, linear uniform filter. Fig. 4.8d shows a PPCC plot from a vertical edge in the blurred image in Fig. 4.8c and the maximum about $\lambda_{max} \simeq 1$ implies a uniform functional form. Hence, the PPCC plots do distinguish between different blurs.

(a) (b) (c) (d)

Figure 4.10: (a) Result from SJA non-blind deconvolution on noisy Lena image using a 12x12 Gaussian blur kernel with $\sigma = 2.6$ (see inset) from the edge profile PSF estimation. (b) Result from SJA non-blind deconvolution using the Fergus's PSF estimation (see inset). (c) Result from SJA blind deconvolution. Inset shows estimated PSF. (d) Result from Cho's Fast blind deconvolution. Inset shows estimated PSF.

Let's look in more detail at analyzing the image in Fig. 4.8a. Automatically finding several high contrast edges, extracting these edge intensity profiles, and finding λ_{max} via the PPCC plot gives a range of $0.05 < \lambda_{max} < 0.15$ for these edges. Or one can obtain an average of the λ_{max}, σ, and length parameters over many strong edges. Doing this gives $\lambda_{max} = 0.1, 0.15, \sigma = 5.1, 5.6$, length $= 26.5, 27$ for vertical and horizontal edges, respectively. In both methods, the results imply a 27x27 Gaussian blur kernel, with $\sigma \simeq 5.4$. This exercise illustrates that for images where a constant PSF assumption is valid, using a few strong edges will typically give similar results to averages over many edges but at a fraction of the computation time.

Fig. 4.9 shows four of the deblurred results of the image in Fig. 4.8a. It is easy to spot the differences in the blur kernels (inset in each image) but it is difficult to accurately compare the relative quality of the deconvolution results because the results are visually quite similar. But we can make a few observations. The SJA programs do provide a smoothing parameter and some experimentation was performed. The value of the current setting was necessary to remove image artifacts but the SJA results appear somewhat over-smoothed relative to other deblurred results The LR deconvolutions contain some ringing artifacts near the image boundaries even though the function edgetaper was used as recommended by Matlab for minimizing this effect. The non-blind results using the Gaussian PSF seem a bit sharper than the results using the Fergus PSF or the blind deconvolution results.

Using the original Lena image as a reference, the quality of these images can be reduced to numerical values and then compared. The fourth column in Table 4.2 lists the mean SSIM values for a variety of PSF and deconvolution combinations, where the blurry Lena gives a score of SSIM = 0.680. Based on the SSIM score, the edge profile PSF estimation produced somewhat better deblurred results than Fergus's method or the blind deconvolution methods. As in the camerman example, this makes sense because this test case is designed to match the underlying assumptions of Section 3.3.

The edge profile method is affected by noise and here we contrast the relative performance of this method to other methods. The standard Lena image was blurred with a Gaussian blur kernel with $\sigma = 3$ and random, Gaussian white noise was added. Using the original Lena image as the reference, this noisy Lena gives a score of SSIM = 0.810. Automatically finding several high contrast edges, extracting these edge intensity profiles, and finding λ_{max} via the PPCC plot gives $\lambda_{max} \simeq 0.15$ but with a larger range of $-0.05 < \lambda_{max} < 0.3$ than the range from processing the purely blurry image. Or one can obtain an average over many strong edges of $\lambda_{max} = 0.15, \sigma = 2.5$, and length $= 11$. In this case it is reasonable to choose the Gaussian functional form, however when the image is polluted by noise there is increased uncertainty since range of these parameters is larger. As in the cameraman image case, manual edge profile extraction produces more accurate results, which

indicates the need for an improved automatic profile extraction methodology. Hence, a 13x13 Gaussian blur kernel, with $\sigma = 2.6$ was used as input to the non-blind deconvolution methods. The deblurred image is shown in 4.10a and the SSIM results shown in column four of Table 4.2.

The Fergus PSF estimation was run on various sub-regions of about 200x200 pixels and the best result is displayed in Fig. 4.10b. The SSIM results using this PSF as input to the three non-blind deconvolution methods is shown in column four of Table 4.2. The CPU time for running the Fergus method on this sub-region is listed in Table 4.3.

Two blind deconvolution blur kernels and resulting images are shown in Figures 4.10c and 4.10d. As the SSIM scores in Table 4.2 shows, the Radon transform, RadonMAP, and SJA blind deconvolution are able to produce results of similar quality to those produced using the edge profile PSF. The other methods' scores suffer due to the presence of noise.

The CPU times for the various software is listed in Table 4.3. Again this Matlab implementation of edge profile method executes orders of magnitude faster than any other method. This speed advantage is one of the core advantages of the edge profile method. This method is valuable as a quick "back-of-the-envelope" estimation of the blur kernel as a check on, or an initial estimate of the kernel for more accurate methods, or simply to obtain an approximate PSF.

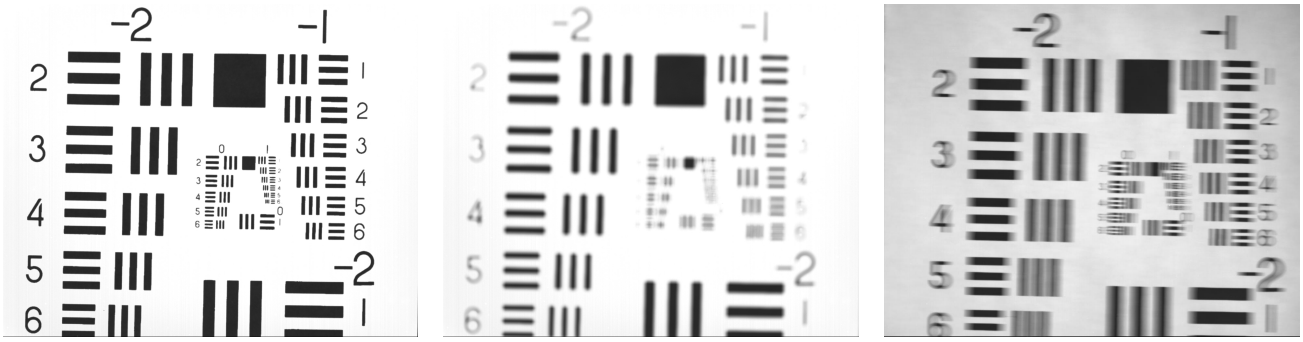

(a) (b) (c)

Figure 4.11: (a) Focused NIR bar chart image. (b) Unfocused NIR bar chart image. (c). Camera motion blurred NIR bar chart image.

4.4 NIR Bar chart imagery

In most real world imagery the functional form of the PSF is unknown. Fig. 4.11a contains images of a focused bar chart in the NIR (wavelengths = 300 - 1100 nm, 1024x1280 pixels). A defocused image is shown in Fig. 4.11b and blur from camera motion is shown in Fig. 4.11c.

Let's first examine the case of the defocused image. Finding λ_{max} for four strong edges gives a range of $0.15 < \lambda_{max} < 0.3$. Or one can obtain an average of the λ_{max}, σ, and length parameters over many strong edges, which gives $\lambda_{max} = 0.25, \sigma = 3.8$, length = 18. The $\lambda_{max} = 0.25$ falls in between the Gaussian and U-shaped functional forms. Tests determined that a Gaussian function had higher SSIM scores than the U-shaped functional form and $\sigma = 3.0$ had a higher score than $\sigma = 3.8$, so a 17x17 Gaussian blur kernel, with $\sigma = 3.0$ was used as input to the deconvolution methods. The SSIM results using this PSF as input to the three non-blind deconvolution methods is shown in column two of Table 4.4. Also, Fig. 4.12a shows the blur kernel and the deconvolution result.

The Fergus PSF estimation was run on various sub-regions of about 200x200 pixels and the best result is displayed in Fig. 4.12b. The results from the edge profile method indicates that the constant PSF assumption is valid for this imagery. The image was obtained by purposely not focusing the camera, which should imply the same blur throughout and a constant PSF should be a reasonably valid assumption. The Fergus PSF result is visibly quite different than a simple Gaussian, yet when the Fergus PSF is used as input to the three non-blind deconvolution methods, the results are similar. The SSIM results using this PSF as input to the three non-blind

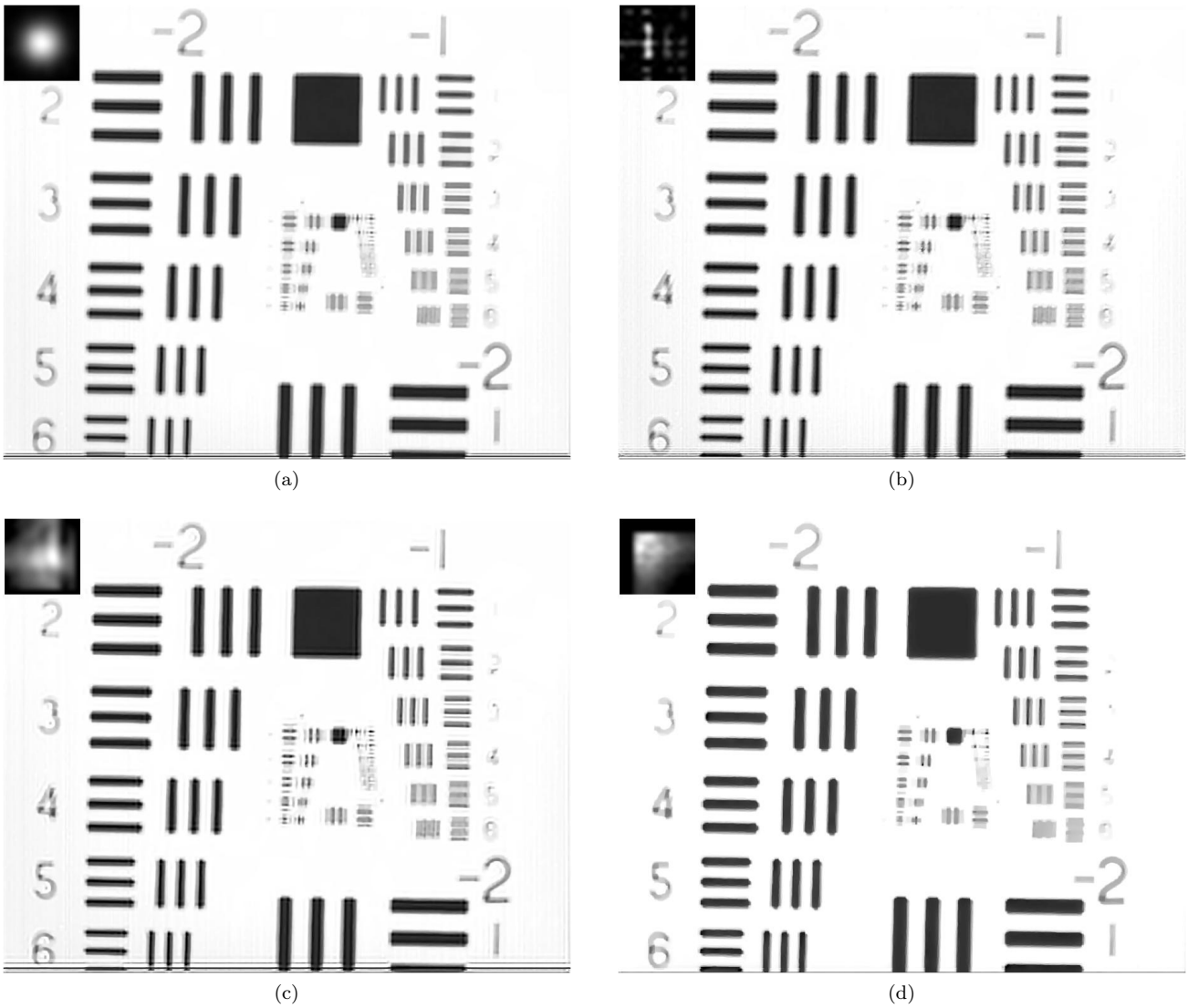

Figure 4.12: (a) Result from SJA non-blind deconvolution using a 17x17 Gaussian blur kernel with $\sigma = 3$ (see inset), determined from the edge profile PSF estimation. (b) Result from SJA non-blind deconvolution using the Fergus's PSF estimation (see inset). (c) Result from SJA blind deconvolution. Inset shows estimated PSF. (d) Result from Cho's Fast blind deconvolution. Inset shows estimated PSF.

deconvolution methods is shown in column two of Table 4.4. Fig. 4.12b shows the deconvolution result and the CPU time for running the Fergus method on this sub-region is listed in Table 4.3.

Two blind deconvolution blur kernels and resulting images are shown in Figures 4.12c and 4.12d. While each blur kernel looks unique, the deconvolved images appear similar. Furthermore, these images all have similar SSIM scores. Hence the major distinction between all of these methods is CPU time, which is listed in Table 4.3 and the edge profile method executes in a fraction of the time of the other methods.

Now let us examine the case of blurring by camera motion. Fig. 4.11c contains an image of the NIR bar chart blurred by camera motion. A PPCC plot of a vertical edge is shown in Fig. 4.13a along with the corresponding intensity profile that was used to create the PPCC plot. This vertical edge has a $\lambda_{max} = 1$ but the horizontal edges have a $\lambda_{max} = 0$, as can been seen by looking at a λ map of a sub-region that is shown in Fig. 4.13b. A comparison of the lengths of vertical versus horizontal edge profiles also illustrate this asymmetry; vertical edge profiles span about 30 to 38 pixels while a horizontal edge profile is only around 4 to 6 pixels. Essentially this

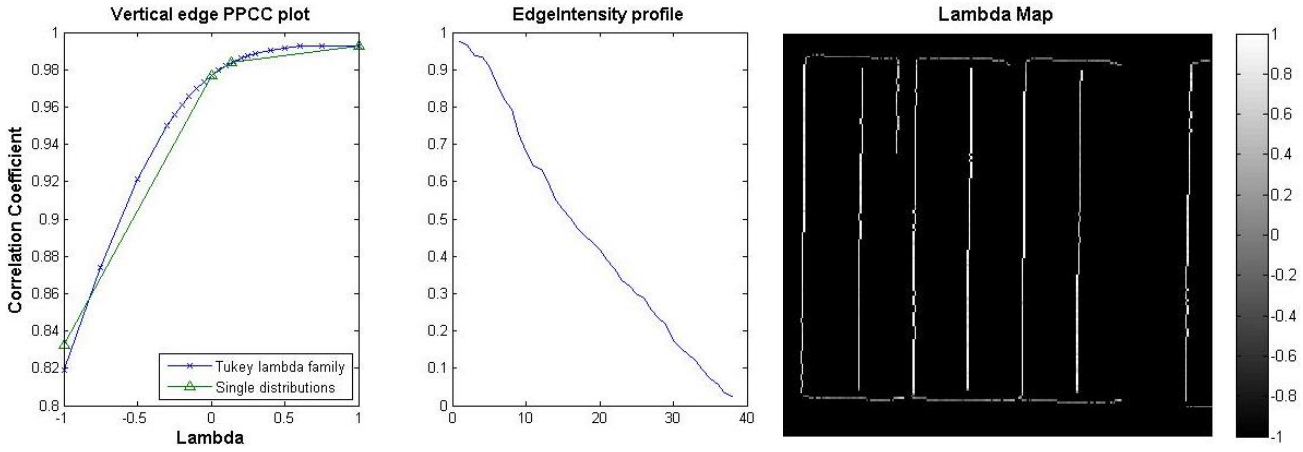

(a) (b)

Figure 4.13: (a) Edge intensity profile and PPCC plot for a vertical edge from image shown in Fig. 4.11c. (b) λ Map of bar chart with camera motion. Shows that $\lambda \simeq 1$ for vertical edges and $\lambda \simeq 0$ for horizontal edges.

Table 4.4: Mean SSIM quality metric of the deblurred images relative to an idealized reference.

Technique	Unfocused NIR	Motion NIR	SWIR	MWIR	Active IR
No deblurring	0.772	0.728	0.819	0.839	0.623
Edge profile PSF / RL	0.803	0.772	0.864	0.894	0.743
Edge profile / Sparse 1	0.806	0.756	0.856	0.885	0.698
Edge profile / Sparse 2	0.781	0.865	0.860	0.847	0.668
Edge profile/SJA non-blind	0.778	0.712	0.833	0.014	0.660
Fergus PSF / RL	0.798	0.726	0.795	0.880	0.630
Fergus PSF / Sparse 1	0.817	0.782	0.853	0.885	0.632
Fergus PSF / Sparse 2	0.780	0.732	0.800	0.878	0.620
Fergus PSF / SJA non-blind	0.770	0.678	0.705	0.013	0.646
Radon transform / Sparse 1	0.784	0.758	0.833	NA	0.691
Radon transform / Sparse 2	0.777	0.858	0.907	NA	0.664
RadonMAP / Sparse 1	0.832	NA	0.831	NA	0.693
RadonMAP / Sparse 2	0.777	NA	0.901	NA	0.664
SJA blind deconvolution	0.759	0.617	0.735	0.016	0.647
Cho's blind deconvolution	0.784	0.721	0.792	NA	0.584

implies a horizontal, uniform, linear PSF of length 30 to 38 pixels (obviously σ is not relevant for a uniform blur kernel). A few tests showed that a linear blur kernel of length 31 produced better results than longer kernels so this is the kernel used to produce the result shown in Fig. 4.14a. Furthermore, comparisons of LR and sparse deconvolution results using 1-D Uniform, U-shape, Gaussian, and logistic PSFs of various sizes showed that a 33 pixel uniform function produces the sharpest edges, which confirms this result. The SSIM scores for deconvolution with this kernel is given in column two of Table 4.4. The scores for the edge profile estimated

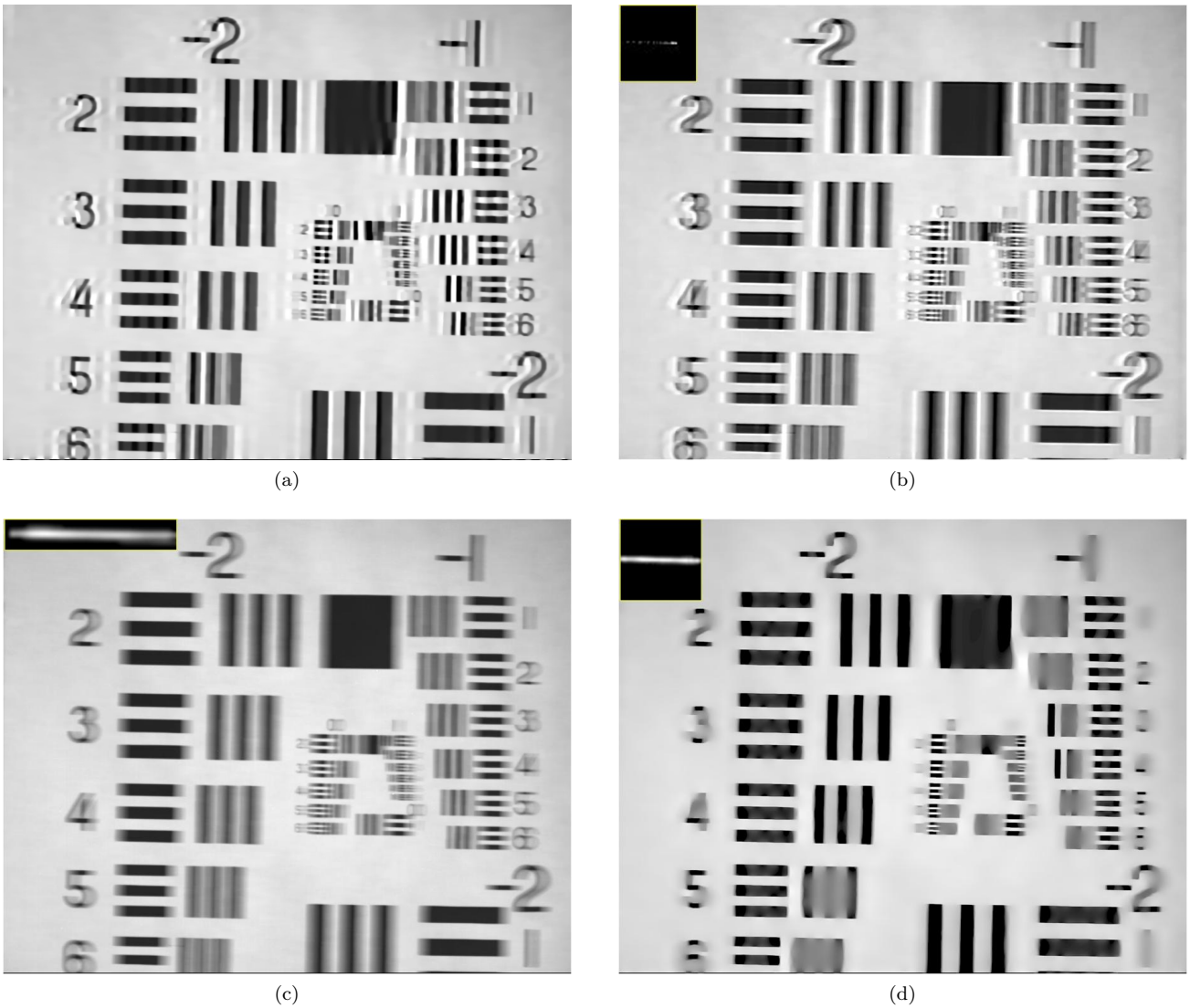

(a) (b) (c) (d)

Figure 4.14: (a) Result from SJA non-blind deconvolution using a 33 pixel, uniform, linear blur kernel as determined from the edge profile PSF estimation. (b) Result from SJA non-blind deconvolution using the Fergus's PSF estimation. (c) Result from SJA blind deconvolution. (d) Result from Cho's Fast blind deconvolution.

Table 4.5: Mean SSIM metric of the motion blurred image using the Radon transform PSF of various values for sliceSize (from 29 to 45) with the two sparse deconvolution methods. Significantly different results were obtained from the sparse deconvolution of [8] than the original implementation by [22].

Technique	29	31	33	35	37	39	41	43	45	47	49
Sparse 2 [8]	0.871	0.883	0.845	0.879	0.880	0.782	0.863	0.757	0.790	0.737	0.765
Sparse 1 [22]	0.753	0.758	0.738	0.728	0.760	0.727	0.734	0.701	0.758	0.745	0.760

PSFs are similar to the other methods in spite of the ringing and ghosting artifacts in the edge profile result and is perhaps helped by some smoothing by the non-blind deconvolution method.

The Fergus, Radon Transform, RadonMAPP, SJA and Cho's fast blind deconvolution methods are all geared

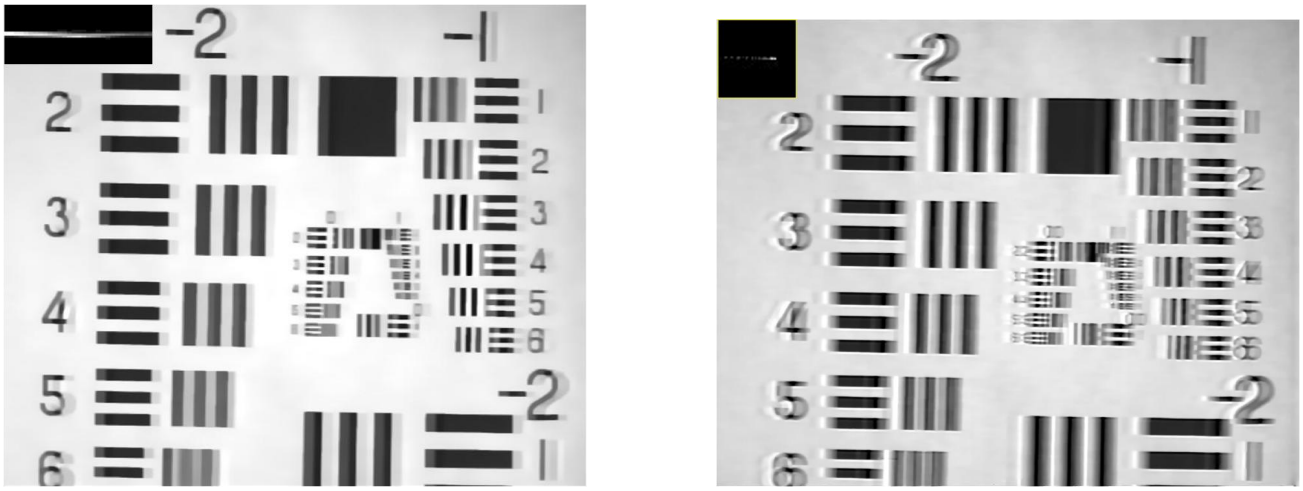

(a) (b)

Figure 4.15: (a) Result from Sparse non-blind deconvolution using a 31x31 Radon transform blur kernel (see inset). (b) Result from SJA non-blind deconvolution using the Fergus's PSF estimation (see inset).

towards deblurring camera shake that causes motion blur. Hence, it should be expected that these methods perform well for this imagery. However, the SSIM scores for the results of deblurring this image, which are given in column two of Table 4.4, show that the simple edge profile PSF obtains comparable results. On the other hand, close examination of the deblurring results of this linear filter to the other deconvolution results show that the edge profile results contain sharper edges but also more ringing and ghosting artifacts. This result illustrates an important difference between this edge profile blur kernel estimation and other methods. Previous PSF estimation and blind deconvolution methods have the dual aims to restore edge sharpness and noise/artifact suppression in homogeneous regions; however, the only goal inherent in the edge profile method is restoring edge sharpness, ideally to step-edges. That is, the results of non-blind deconvolution for the edge profile blur kernel tends to have have both sharper edges and more artifacts than the other methods.

The Fergus PSF estimation was run on various sub-regions of size about 200x200 and the best result is displayed in Fig. 4.15b. The estimated PSF is nearly linear and yet it seems this PSF does only a little to sharpen edges. Fig. 4.14c presents the deblurring results for the SJA blind deconvolution method and here it is clear the estimated PSF is nearly linear. Similarly for Cho's fast blind deconvolution results shown in Fig. 4.14d, however the method seems to over smooth parts of the image and appears to be of poor quality. Also, keep in mind that it is likely that the scores for the edge profile estimated PSFs are lowered because of the ringing and ghosting artifacts.

This image was input to the Radon transform method and the results were somewhat inexplicable. When the method was run with the original code, including their sparse deconvolution, the resulting image was significantly better than any other method (see Fig. 4.15a). However, saving the same PSF and running with Levin's sparse deconvolution produced poor results. This can be seen in the results contained in column three of Table 4.4 and even more clearly in Table 4.5, which compares the two sparse deconvolution methods over a range of sliceSize values. I examined the code and experimented with a variety of parameters values, yet was not able to explain these results. Furthermore, there does not seem to be a logical pattern in Table 4.5 correlating the SSIM value to the values of sliceSize. However, some of the better SSIM values using the sparse deconvolution of [8] were obtained for sliceSize in the range of 31 to 37, which corresponds nicely to the length of the edge profiles cited above. Several attempts to run the RadonMAP program failed to complete executing so no results were obtained.

It is also noteworthy that image registration is necessary before computing a SSIM score because the long kernel can significantly shift the edge location relative to the focused reference image. Subsequently, sub-pixel registration method was then used to obtain SSIM scores for all the imagery in Tables 4.2 and 4.4, even though for most of the other imagery the shift was small.

(a) (b)

Figure 4.16: (a) Focused SWIR image. (b) Unfocused SWIR image.

(a) (b) (c) (d)

Figure 4.17: (a) Result from SJA non-blind deconvolution using an 11x11 logistical blur kernel with $\sigma = 1.5$ (see inset), as determined from the edge profile PSF estimation. (b) Result from SJA non-blind deconvolution using the Fergus's PSF estimation (see inset). (c) Result from SJA blind deconvolution. Inset shows estimated PSF.

4.5 Outdoor SWIR imagery

Fig. 4.16a shows a focused SWIR image (wavelengths = 0.9 - 1.7 um, 700x550 pixels) and Fig. 4.16b shows an unfocused version of the same scene. Finding λ_{max} for four strong edges gives a range of $0 < \lambda_{max} < 0.2$. Or one can obtain an average of the λ_{max}, σ, and length parameters over many strong edges, which gives $\lambda_{max} = 0.2, \sigma = 3$, length = 11. The $\lambda_{max} \simeq 0.2$ implies the Gaussian functional form with $\sigma = 3.0$, which tests confirm. For the results given in this section, a 13x13 Gaussian with $\sigma = 3.0$ was used. The SSIM results using this PSF as input to the four non-blind deconvolution methods is shown in column four of Table 4.4. Also, Fig. 4.17a shows the blur kernel and the deconvolution result.

The Fergus PSF estimation was run on various sub-regions of about 200x200 pixels and the best result is displayed in Fig. 4.17b. The Fergus PSF result is visibly quite different than a simple Gaussian, yet when the Fergus PSF is used as input to the non-blind deconvolution methods, the results are quite similar. The SSIM results using this PSF as input to the four non-blind deconvolution methods are also shown in column four of Table 4.4. Fig. 4.17b shows the deconvolution result and the CPU time for running the Fergus method is listed in Table 4.3. The Radon transform and RadonMAP methods both work well and produce good quality results.

Two blind deconvolution blur kernels and resulting images are shown in Figures 4.17c and 4.17d. These images appear to be very similar and all have similar SSIM scores, as can be seen in Table 4.4. The differences in SSIM scores are more related to the amount of smoothing done by the non-blind deconvolution method rather than related to the differences in the input blur kernel. Hence the major distinction between all of these methods is CPU time, which is listed in Table 4.3. The SWIR image is one of the larger images studied in this research, hence the CPU difference between methods is more pronounced.

4.6 Tests on atmospheric turbulence blurred imagery

Applying these algorithms to real-world imagery is an important test. One ubiquitous cause of blurring is from atmospheric turbulence, which often imposes a practical limit on the performance of imaging sensor systems [28]. Two videos demonstrating atmospheric turbulence blurring effects were provided courtesy of the Night Vision and Electronic Sensors Directorate (US Army RDECOM CERDEC NVESD). The first image sequence was collected at a mid-Atlantic US Army Test Site on September 2008 using a L3/CE 640x512x28μm MWIR sensor, and this video contains distortion and warping along with the blurring. The second is an active IR video sequence recorded at a closed test site, which has significant noise and speckle artifacts. Both these problems are mitigated by averaging several frames; 10 frames for the first sequence and 50 for the second. The averaged images are displayed in Fig. 4.18 and these images were used in the investigations discussed in this section. Although there aren't references for these image, ideal reference images shown in Fig. 4.19 were created in order to compute SSIM values . For the MWIR image the SSIM score of the target area from the original image was computed to be 0.839. The reference for the active IR image consisted of white squares and rectangles on a homogeneous dark background and an effort was made to align the reference with the image. The SSIM score of the the image in Fig. 4.18 to this reference is 0.623.

MWIR imagery

Automatic extraction of the edge profiles had some variability, giving a range of results of $0 < \lambda_{max} < 0.3, 2.3 < \sigma < 2.8$, and length between 10 and 14 pixels. However, manual extraction of several edge profiles from Fig. 4.18a gave $\lambda_{max} = 0.1, \sigma = 2.3$, and length of 12 pixels. Either a Gaussian or a logistical function fits within this range and our tests showed that the logistical blur kernel performed a little better than a Gaussian PSF. Fig. 4.20a shows the results of non-blind sparse deconvolution using a 11x11 logistical PSF with $\sigma = 2$.

In Fig. 4.20b is the result of the Fergus PSF estimation and the results of non-blind sparse deconvolution. Examination of the SSIM scores in Table 4.4 show similar results are obtained from both methods. However, as seen in Table 4.3, the CPU times for the edge profile method is a fraction of the time for the Fergus method. Due to the lack of edges in this image, the Radon transform and RadonMAP methods failed in most attempts and when it was possible to produce a result, it was of very poor quality. Attempts to deconvolve this image with SJA blind and non-blind deconvolution produced poor results, which can be seen in Fig. 4.20c and are reflected in the SSIM scores. In addition, it was not possible to obtain a result with Cho's blind deconvolution, even over a range of parameter settings. This image demonstrates the robustness of the edge profile method because it is possible to obtain an approximate blur kernel with difficult imagery; it simply requires manually extracting the profile rather than relying on the automatic profile extraction.

Active IR imagery

The active IR image in Fig. 4.18b is a difficult problem because active IR is prone to significant image artifacts, including noise and speckle effects. It is instructive to examine the λ and σ maps for this image, which are shown in Fig. 4.21. It appears in the map that λ shows significant variation due to noise, which implies that the

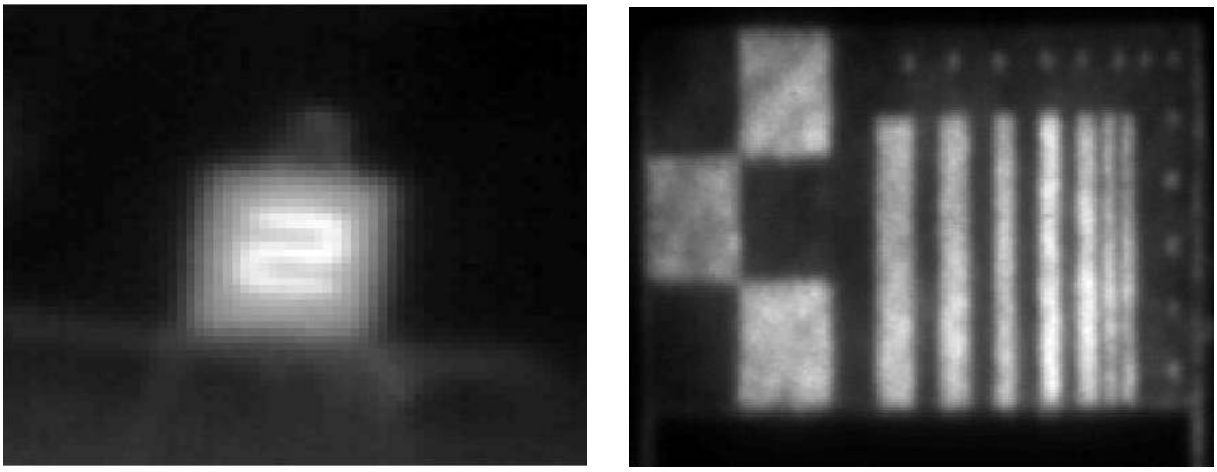

(a) (b)

Figure 4.18: (a) MWIR collect at a US Army Test Site on September 2008. Displayed image is an average of the first 10 frames. (b) Displayed image is a sub-region containing one of the targets from a closed test site. It was taken with an Active IR sensor. The displayed image is an average of 50 frames to reduce the noise inherent in active IR imagery.

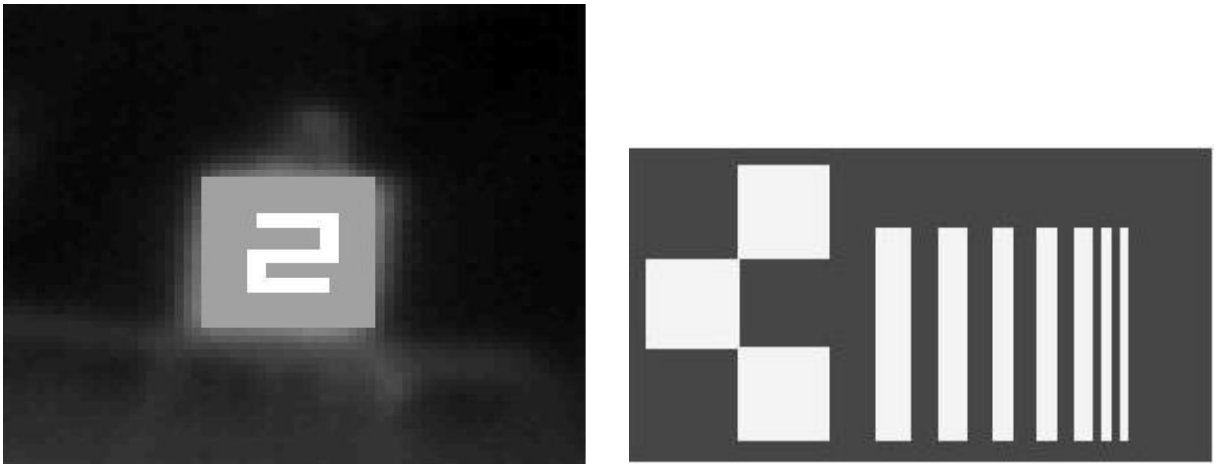

(a) (b)

Figure 4.19: (a) MWIR reference image for SSIM comparison. (b) Active IR reference image.

assumption of a constant blur kernel is poor for this image. But the constant PSF assumption was used for the sake of continuing the comparison with the deconvolution methods used so far in this report.

Finding λ_{max} for four strong edges gives a wide range of $-0.05 < \lambda_{max} < 0.25$, where each of these four edge gave a different value. Closer examination of the results indicates that the best edge profile gives $\lambda_{max} = 0.05$. Looking at averages from the automatic evaluation of the edge profiles in the image gives $\lambda = 0.05$ and an average value of σ is in the range from 2.0 to 2.9. Manual extraction of several edge profiles give $\lambda_{max} = 0.05$ to $0.1, \sigma = 2.3$, and length of 13 to 15 pixels., which can imply either a Gaussian or logistic functional form. Tests show that either functional form produced similar results but the logistical function requiring a larger value for σ of approximately 3.0. So a 13x13 Gaussian blur kernel with $\sigma = 2.4$ was used to produce the result in Fig. 4.22a.

In Fig. 4.22b is the result of the Fergus PSF estimation and the results of non-blind SJA deconvolution. Also, Table 4.3 gives a comparison of the CPU times, where the edge profile method again requires a fraction of the time the other methods need. Two blind deconvolution blur kernels and resulting images are shown in Figures

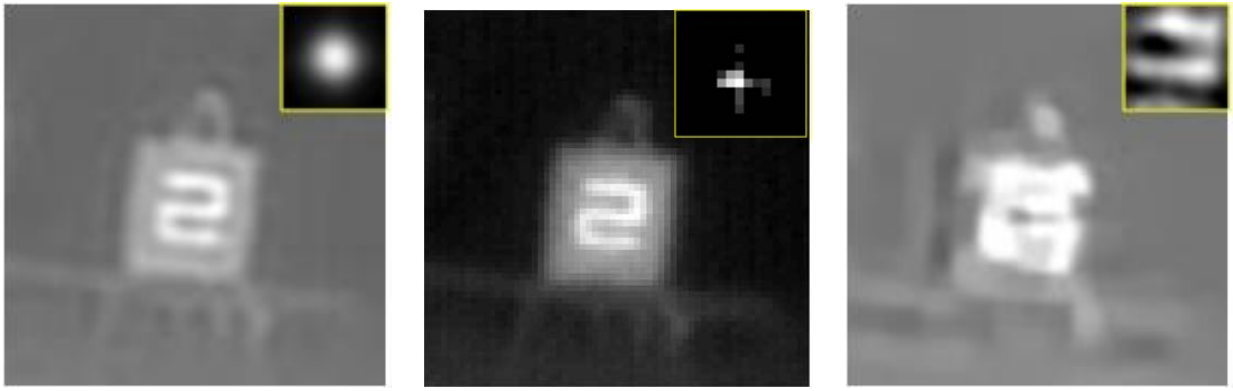

(a) (b) (c)

Figure 4.20: PSF estimation (corner insert) and non-blind sparse deconvolution for the MWIR image. (a) Edge profile estimation of a 11x11 logistical blur kernel. (b) Fergus PSF estimation. (c) SJA blind deconvolution.

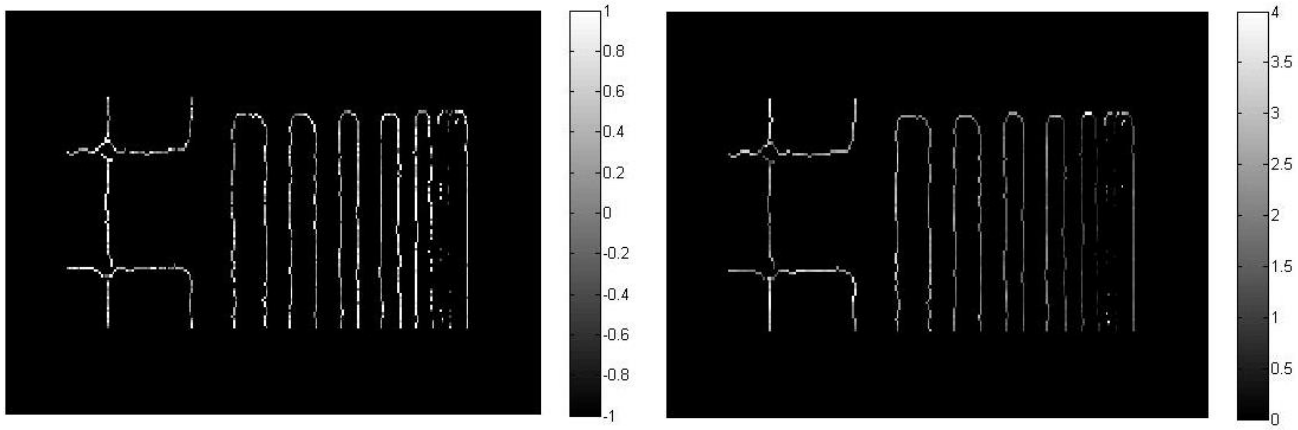

(a) (b)

Figure 4.21: (a) λ map for Active IR image. (b) σ map.

4.22c and 4.22d. The Radon transform and RadonMAP methods were also run on this image and the results appear visually similar to the Fergus PSF results but the SSIM scores in Table 4.4 are somewhat higher. It can be seen that the SSIM values in column five of Table 4.4 also are similar, so once again it is the CPU time that primarily differentiates the methods.

The inconsistency of the results shown in Fig. 4.22 and SSIM scores in Table 4.4 require some discussion. Cho's fast deblurring method obtains a relatively high SSIM score but the image displayed in Fig. 4.22d is visibly of poorer quality than the other images. This is caused by the simple choice for a reference image to use homogeneous light regions on a homogeneous dark background. The smoothing performed by Cho's fast deblurring method creates a result that most resembles this reference. There might be times when this result is desirable but for our purposes this seems to be a poor visual result. The results in Figures 4.22a and 4.22b again illustrate the difference between this edge profile blur kernel estimation and other methods; that is, other methods have the dual aims to restore edge sharpness and noise/artifact suppression in homogeneous regions, while the only goal inherent in the edge profile method is restoring edge sharpness.

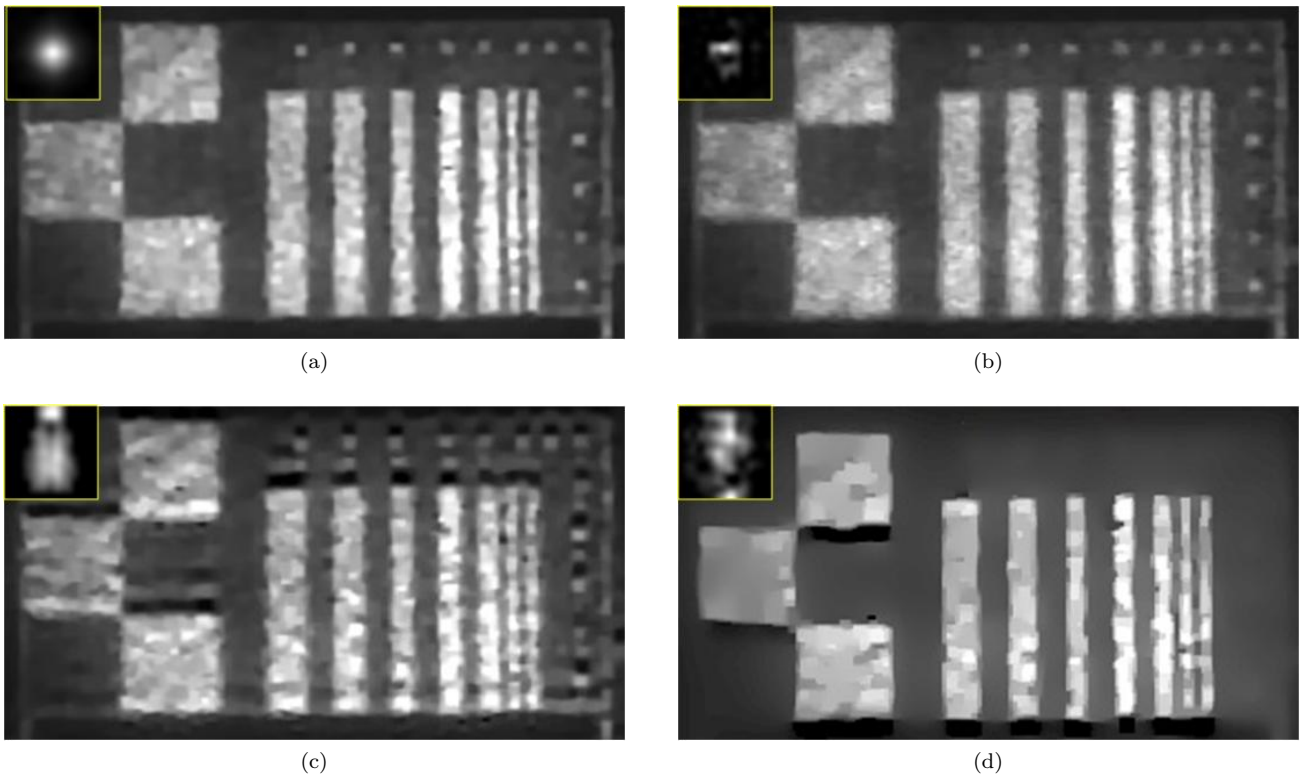

(a) (b) (c) (d)

Figure 4.22: (a) Result from SJA non-blind deconvolution using a 15x15 logistic blur kernel with $\sigma = 3$ (see inset), as determined from the edge profile PSF estimation. (b) Result from SJA non-blind deconvolution using the Fergus's PSF estimation (see inset). (c) Result from SJA blind deconvolution. Inset shows estimated PSF. (d) Result from Fast blind deconvolution. Inset shows estimated PSF.

4.7 Limitations

As with any methodology, there are boundaries beyond which this approach is not practical. It is outside the capability of the edge profile method to determine random blur kernels found in the camera motion deblurring literature such as [7], [16], [15], [21]. Furthermore, initial tests with imagery blurred by these complex blur kernels showed that the edge profile method performed poorly relative to the Fergus method. The complex kernels in the motion blur literature generally have non-analytic shapes, random values and are not symmetrical. Hence, based on the assumptions described in Section 3.3, this is beyond the capability of this method. On the other hand, it is possible to use a fast edge profile PSF estimation for an initial guess to be input into more accurate PSF estimation or blind deconvolution techniques, such as in [7], [16], [15], [21], in order to produce faster and flexible techniques. This topic is a candidate for future research.

As mentioned above, the edge profile method aims only to sharpen edges while other methods have the dual goals of sharper edges and reducing noise/artifacts in smooth regions. In addition, there are some approximations in the automation of this method that may introduce errors and limit the accuracy of the result in the presence of noise. For example, this method relies primarily on differences between shapes of the profile. During this study it was noticed that the greater the blurring or more noise present, the more difficult it is to distinguish between functional forms. This effect was present in the results described in Sections 4.2 and 4.6. On the other hand, in these cases the deconvolution results from different functional forms are similar and the edge profile method still provides reasonable parameter values.

Furthermore, the methods for determining the endpoints of the blurry edge profile are approximate and an incorrect edge profile can introduce error into blur kernel estimates. Also, for the work presented in this report, noise hindered the automatic endpoint estimation and occasionally required manual edge profile extraction. However, it is hoped that the automated implementation will become more robust in the course of time.

Chapter 5

Conclusions

This report shows how to estimate the blur kernel directly from a blurry image by using the concepts behind quantile-quantile plots, probability plots, and probability plot correlation coefficient plots. Finding the shape parameter that yields the maximum probability plot correlation coefficient indicates the best functional form for the blur kernel. Given the functional form of the blur kernel, the parameters are obtained from a straight line fit to the transformed edge profile, eliminating any searching of the parameter space. Maps provide insight to the asymmetry and spatial variation in an image's blurring, allowing an informed decision on whether to use an isoplanatic or anisoplanatic, symmetric or asymmetric PSF. These methods are non-iterative, simple, and robust to noise.

Although most of the Results section is spent comparing the edge profile method to state-of-the-art methods, this method is best compared to PSF selection by standard models. In the standard model method one guesses at a functional form and parameters based on a prior knowledge of the blurring or one searches the parameter space to estimate the parameters. Instead, the edge profile method shows how to quickly estimate the functional form and parameters from blurry edges in the image. We show in the Results section that a blur kernel estimated in such a simple manner produces deconvolution results of similar quality to the results from much more computationally intensive state-of-the-art deconvolution methods.

This work opens up several areas for future research. One area is to obtain more versatile and accurate blur kernels through the use of other blur functions or a mixture of functions [26] [25]. Secondly, the edge profile method can be integrated with a more accurate PSF estimation or blind deconvolution method. Finally, integrating the edge profile method with a spatially varying deconvolution method will take advantage of both its qualities of speed and locality.

Image deblurring is a building block for many other techniques. Atmospheric turbulence mitigation was studied in this report but this methodology could be applied to a number of applications. For example, this method is particularly suited for the deblurring step of super-resolution methods because it defines a continuous function for the blur kernel, and hence can be defined at any desirable resolution.

Acknowledgment

The author would like to thank the Office of Naval Research for their support of this research and Richard Espinola at US Army RDECOM CERDEC NVESD for supplying the imagery used in this investigation. In addition, the author thanks Colin Olson of NRL for his comments on this report and all the researchers who made their programs available.

Bibliography

[1] Hugh G. Gauch, *Scientific method in practice*, Chapter 7, Cambridge University Press, 2003.

[2] Richard W. Hamming, *The art of doing science and engineering : learning to learn*, Chapter 1, Gordon and Breach, 1997.

[3] Reginald L. Lagendijk and Jan Biemond, *Basic Methods for Image Restoration and Identification*, Chapter 3.5, Handbook of image and video processing, Editor Al Bovik, Academic Press, 2000.

[4] D. Kundur and D. Hatzinakos, "Blind image deconvolution", IEEE Signal Processing Magazine, 1996.

[5] Anat Levin, Yair Weiss, Fredo Durand, William T. Freeman, "Understanding and evaluating blind deconvolution algorithms", IEEE Computer Society Conference on Computer Vision and Pattern Recognition, CVPR'09, 2009.

[6] Leslie N. Smith, James R. Waterman and K. Peter Judd, "A new blur kernel estimator and comparisons to state-of-the-art", Proc. SPIE 8014, 80140N (2011); doi:10.1117/12.888126.

[7] R. Fergus, B. Singh, A. Hertzmann, S.T. Roweis, and W.T. Freeman " Removing camera shake from a single photograph", SIGGRAPH, 2006.

[8] Taeg S. Cho, Sylvain Paris, Berthold K.P. Horn, William T. Freeman, "Blur kernel estimation using the Radon transform", IEEE Computer Society Conference on Computer Vision and Pattern Recognition, CVPR'11, 2011.

[9] N. Joshi, R. Szeliski, and D. Kriegman, "PSF estimation using sharp edge prediction", IEEE Computer Society Conference on Computer Vision and Pattern Recognition, CVPR'08, 2008.

[10] Ming-Chao Chiang, Terrance E. Boult, "Local Blur Estimation and Super-Resolution", IEEE Computer Society Conference on Computer Vision and Pattern Recognition (CVPR'97), pp.821, 1997.

[11] E.H. Barney-Smith, "PSF estimation by gradient descent fit to the ESF", SPIE Image Quality and System Performance III,Vol. 6059, 2006.

[12] V. Kayargadde and J.-B. Martens, "Estimation of edge parameters and image blur using polynomial transforms", CVGIP Graphical Models Image Process., 56, 442461, 1994.

[13] B. Chalmond, "PSF Estimation for Image Deblurring", CVGIP: Graphical Models and Image Processing, Vol. 53, No. 4, pp. 364-372, 1991.

[14] Azriel Rosenfeld, Avinash Kak, *Digital Picture Processing*, Academic Press, 1982.

[15] Q. Shan, J. Jia, A. Agarwala, "Highquality Motion Deblurring from a Single Image", ACM Trans. Graph. 27, 3, Article 73, August 2008.

[16] Sunghyun Cho, Seungyong Lee "Fast Motion Deblurring", Proceedings of SIGGRAPH ASIA , 28, 5, December 2009.

[17] T. J. Schulz, "Multiframe blind deconvolution of astronomical images", J. Optical Soc. Amer., 10, pg. 10641073, 1993.

[18] L. Yuan, J. Sun, L. Quan,H. Shum, "Image deblurring with blurred/noisy image pairs", ACM Trans. on Graph. (SIGGRAPH) 26, 3, 110, 2007.

[19] W. Richardson, "Bayesian-based iterative method of image restoration", Journal of the Optical Society of America A 62, 1972.

[20] L. Lucy, "An iterative technique for the rectification of observed distributions", Journal of Astronomy, Volume 79, number 6, pages 745-754, 1974.

[21] L. Yuan, J. Sun, L. Quan,H. Shum, "Progressive Interscale and Intrascale Nonblind Image Deconvolution", ACM Trans. Graph. 27, 3, Article 74, August 2008.

[22] A. Levin, R. Fergus, F. Durand, and W. Freeman, "Image and depth from a conventional camera with a coded aperture", SIGGRAPH, 2007.

[23] James J. Filliben, "The Probability Plot Correlation Coefficient Test for Normality", Technometrics, Vol. 17, No. 1, pp. 111-117 (Feb., 1975).

[24] John Chambers, William Cleveland, Beat Kleiner and Paul Tukey, *Graphical Methods for Data Analysis*, Chapter 6, Wadsworth and Brooks, 1983.

[25] Zaven A. Karian and Edward J. Dudewicz, *Fitting Statistical Distributions: The Generalized Lambda Distribution and Generalized Bootstrap Methods*, CRC Press, 2000.

[26] Warren Gilchrist, *Statistical Modelling with Quantile Functions*, Chapman and Hall/CRC, 2000.

[27] Z. Wang, A. C. Bovik, H. R. Sheikh, and E. P. Simoncelli, "Image quality assessment: From error visibility to structural similarity," IEEE Transactions on Image Processing, vol. 13, no. 4, pp. 600-612, Apr. 2004.

[28] Richard L. Espinola, Jae Cha, and Kevin Leonard, "Novel methodologies for the measurement of atmospheric turbulence effects", Proc. SPIE 7662, 76620W, 2010.

Biography

Leslie N. Smith received a Ph.D. degree in chemical physics from the University of Illinois in 1979. He currently works for the Naval Research Laboratory in Washington, D.C. as a member of the Maritime Sensing Section in the Optical Sciences Division on real-time image processing and target detection, tracking applications. His research interests include real-time video processing, image restoration, image enhancement (high dynamic range compression, contrast enhancement, super-resolution), use of GPUs in image processing, threat detection (image registration, automatic object detection, background modeling, change detection, tracking, object segmentation, classification) and automatic image understanding.